JOURNAL OF GEOPHYSICAL RESEARCH, VOL. 106, NO. E11, PAGES 28,001–28,022, NOVEMBER 25, 2001

Rock types of South Pole-Aitken basin and extent of basaltic volcanism

C. M. Pieters,[1] J. W. Head III,[1] L. Gaddis,[2] B. Jolliff,[3] and M. Duke[4]

Abstract. The enormous pre-Nectarian South Pole-Aitken (SPA) basin represents a geophysically and compositionally unique region on the Moon. We present and analyze the mineralogical diversity across this basin and discuss the implications for basin evolution. Rock types are derived from Clementine multispectral data based on diagnostic characteristics of ferrous absorptions in fresh materials. Individual areas are characterized as noritic (dominated by low-Ca pyroxene), gabbroic/basaltic (dominated by high-Ca pyroxene), feldspathic (<3-6% FeO), and olivine-gabbro (dominated by high-Ca pyroxene and olivine). The anorthositic crust has effectively been removed from the interior of the basin. The style of volcanism within the basin extends over several 100 Myr and includes mare basalt and pyroclastic deposits. Several areas of ancient (pre-Orientale) volcanism, or cryptomaria, have also been identified. The nonmare mafic lithology that occurs across the basin is shown to be noritic in composition and is pervasive laterally and vertically. We interpret this to represent impact melt/breccia deposits derived from the lower crust. A few localized areas are identified within the basin that contain more diverse lithologies (gabbro, olivine-gabbro), some of which may represent material from the deepest part of the lower crust and perhaps uppermost mantle involved in the SPA event.

1. Introduction

The farside of the Moon is quite different from the familiar side of this small planetary body that perpetually faces Earth. The farside is dominated by rough highland terrains with only a few small basalt deposits; it lacks the extensive basaltic plains that have filled most of the low-lying areas of the nearside. The farside also contains the largest and deepest documented impact basin on the Moon: the immense South Pole-Aitken basin, which is more than 8 km deep and extends approximately 2500 km from the south pole to the crater Aitken, located 15° south of the equator (see summaries by *Wilhelms*, [1987]; and *Head et al.* [1993]). Until recently, our view of the Moon has been shaped largely by observations and exploration of the nearside. Data from the Apollo and Luna samples have provided benchmark information about several major rock types of the Moon and the degree to which each represents different stages of lunar evolution. Analysis of lunar samples from several sites on the nearside have lead directly to the development of the concept of a lunar "magma ocean" and the formation of a differentiated crust and mantle. Information from the lunar samples has allowed us to constrain the age and context of many geologic units of the nearside. In contrast, our understanding of the character and evolution of the farside is sketchy. Data obtained recently by the Galileo, Clementine, and Lunar Prospector missions have allowed the first global compositional assessment of material on the lunar farside [e.g., *Belton et al.*, 1992; *Lucey et al.*, 1994; *Lawrence et al.*, 1998]. South Pole-Aitken (SPA) basin can be seen in Figure 1 as a broad, generally circular, low-albedo region on the southern farside. These data suggest South Pole-Aitken is a compositionally unique region on the Moon [e.g., *Pieters et al.*, 1997b; *Lucey et al.*, 1998c; *Jolliff et al.*, 2000]. Several concepts pertaining to the origin of the unusual properties seen at SPA are under close scrutiny: SPA may have excavated through the lunar crust and into the mantle; it may have exposed the lower crustal section; it may have an extensive overprint of melted material and breccia debris from the original and later impacts; early volcanic deposits may have been emplaced and then masked by the same impact processes. Below we describe current issues associated with this enormous South Pole-Aitken basin and in subsequent sections we document the rock types inferred from orbital observations across this basin and discuss implications for basin formation, impact modification, and mare-filling history.

2. Geological Background and Key Issues

The pre-Nectarian South Pole-Aitken basin is the largest and oldest unequivocally recognized and well-documented impact basin on the Moon. It occupies a major part of the south central farside. Limited photographic coverage of the farside and the relatively degraded nature of SPA caused it to remain undetected for many years. Only the proposed near-side Procellarum basin is larger (~3200 km) and older [*Wilhelms et al.*, 1979], but Procellarum has not been widely accepted as an impact basin.

The existence of a large farside basin was originally predicted on the basis of the presence of mountains near the nearside South Pole [*Hartman and Kuiper*, 1962], and additional evidence for farside mountain ranges was revealed by Apollo [*Wilhelms*, 1969]. However, it was not until Zond images [*Kislyuk*, 1975; *Rodionov et al.*, 1971, 1976; *Shevchenko*, 1980; *Shpekin*, 1983]

[1]Department of Geological Sciences, Brown University, Providence, Rhode Island, USA.
[2]U.S. Geological Survey, Flagstaff, Arizona, USA.
[3]Department of Earth and Planetary Sciences, Washington University, St. Louis, Missouri, USA.
[4]Lunar and Planetary Institute, Houston, Texas, USA.

Paper number 2000JE001414.
0148-0227/01/2000JE001414$09.00

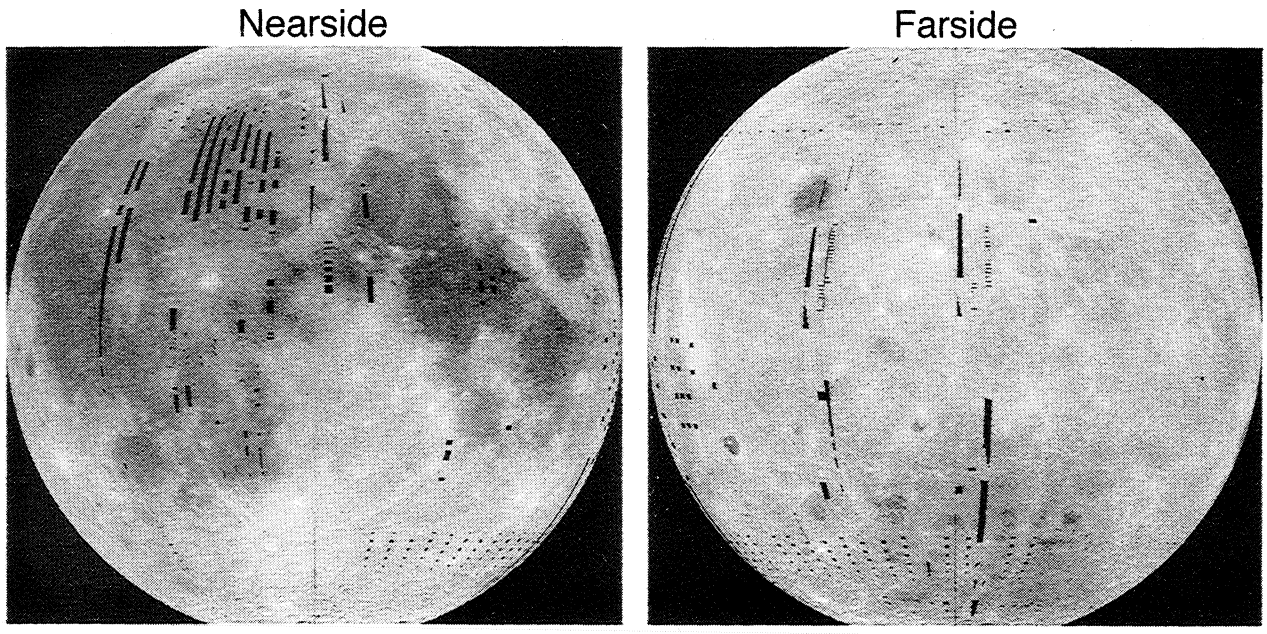

Figure 1. Global mosaic of the Moon prepared from Clementine 750 nm images [*Eliason et al.,* 1999a, 1999b]. On the left is the nearside hemispheric view centered at 0°; on the right is the farside hemispheric view centered at 180°W. Both views are in the orthographic projection.

and Apollo laser altimetry [*Wollenhaupt and Sjogren*, 1972a, 1972b; *Kaula et al.*, 1973] demonstrated the presence of a huge depression (~ 5-7 km deep) that the previous observations were integrated into the concept of a major impact basin [*Howard et al.*, 1974; *Stuart-Alexander*, 1978; *Wilhelms et al.*, 1979; *Leikin and Sanovich*, 1985]. Apollo gamma ray spectroscopy across the northern part of the basin demonstrated that its iron content is enriched relative to the surrounding highlands [*Metzger et al.*, 1974; *Stuart-Alexander*, 1978]. Initial analysis of Galileo images revealed that the basin interior also has a strong 1 μm absorption interpreted to be due to abundant mafic minerals, possibly originating by impact excavation of lower crust or mantle material or from later maria (cryptomaria) [*Belton et al.*, 1992; *Head and Wilson*, 1992]. The regional extent of this major anomaly associated with the South Pole-Aitken basin region is recognized readily in Galileo color-ratio composite images of the southern farside [*Belton et al.*, 1992].

Because of the extremely large size and degraded nature of the basin, the exact diameter of the structure and the location of its rings are a matter of debate. *Stuart-Alexander* [1978] proposed that the basin is 2000 km in diameter and centered at -50°, 180°, while *Wilhelms et al.* [1979] map a basin 2500 km in diameter and centered at -56°, 180°, and a possible inner ring 1800-2000 km in diameter is proposed by *Wilhelms et al.* [1979]. *Wood and Gifford* [1980] mapped 28 possible rim segments and estimated a diameter of ~ 2600 km with a center at -60°S, 180°E. They point out, however, that the rim suggested by the Apollo altimetry [*Wollenhaupt et al.*, 1973] is 300-600 km larger than the rim they define morphologically. Finally, *Leikin and Sanovich* [1985] used Zond 8 data to produce a N-S profile at about -150° and, combined with Apollo 15 and 17 altimetry, determined a basin diameter of 2200 km centered on -41.5°S, 183.5°E. We adopt the two diameter estimates and center positions proposed by *Stuart-Alexander* [1978] and *Wilhelms et al.* [1979] in this discussion.

Additional early evidence supporting the presence of the basin is found in the paucity of craters >25 km in diameter in the interior relative to the exterior [*Wood and Gifford*, 1980] and in the concentration of mare deposits and associated volcanic features [*Scott et al.*, 1977] compared to other farside regions. Virtually all mapped mare deposits in the South Pole-Aitken basin occur within post-South Pole-Aitken craters and basins, and are mapped as Upper Imbrian or Eratosthenian in age [*Stuart-Alexander*, 1978; *Wilhelms et al.*, 1979; *Wilhelms*, 1987]. Prior to Clementine, no cryptomaria or pyroclastic material had been mapped in the South Pole-Aitken basin.

On the basis of pre-Clementine data, the South Pole-Aitken basin appeared to be anomalously deep (up to 7-8 km below the adjacent highlands) for a basin of its size and age. Viscous relaxation of basin topography, particularly in the early history of the Moon when the thermal gradient was steeper, together with mare infilling, serve to reduce the initial topography of impact basins [*Solomon et al.*, 1982]. In this fashion, many of the old nearside basins (e.g., Tranquillitatis, Fecunditatis) have lost their long-wavelength topographic expression. *Solomon et al.* [1982] attribute the unusual depth of South Pole-Aitken, which is notably distinct from that of the nearside basins, to a factor of ten difference in nearside-farside crustal viscosities during the pre-Nectarian period when viscous processes were important. A difference of 50°-100°C in the upper crust would be enough to explain the difference in effective viscosities. Thus, during the pre-Nectarian period on the farside, the cooler, more viscous crust could not flow in to shallow the basin as it did on the nearside. The South Pole-Aitken basin is also a major negative free-air gravity anomaly and the Apollo basin (537 km in diameter), lying at ~36°S, 152°W within the basin, may be the location of the largest negative anomaly on the Moon [*Ferrari*, 1977].

A number of large craters and basins are superposed within the SPA basin (e.g., Apollo, Ingenii, Schrödinger, Planck) or on the rim (e.g., Keeler-Heaviside, Australe), commonly obscuring the continuity of the rim structure. These younger basins have clearly deposited their own ejecta within South Pole-Aitken, or

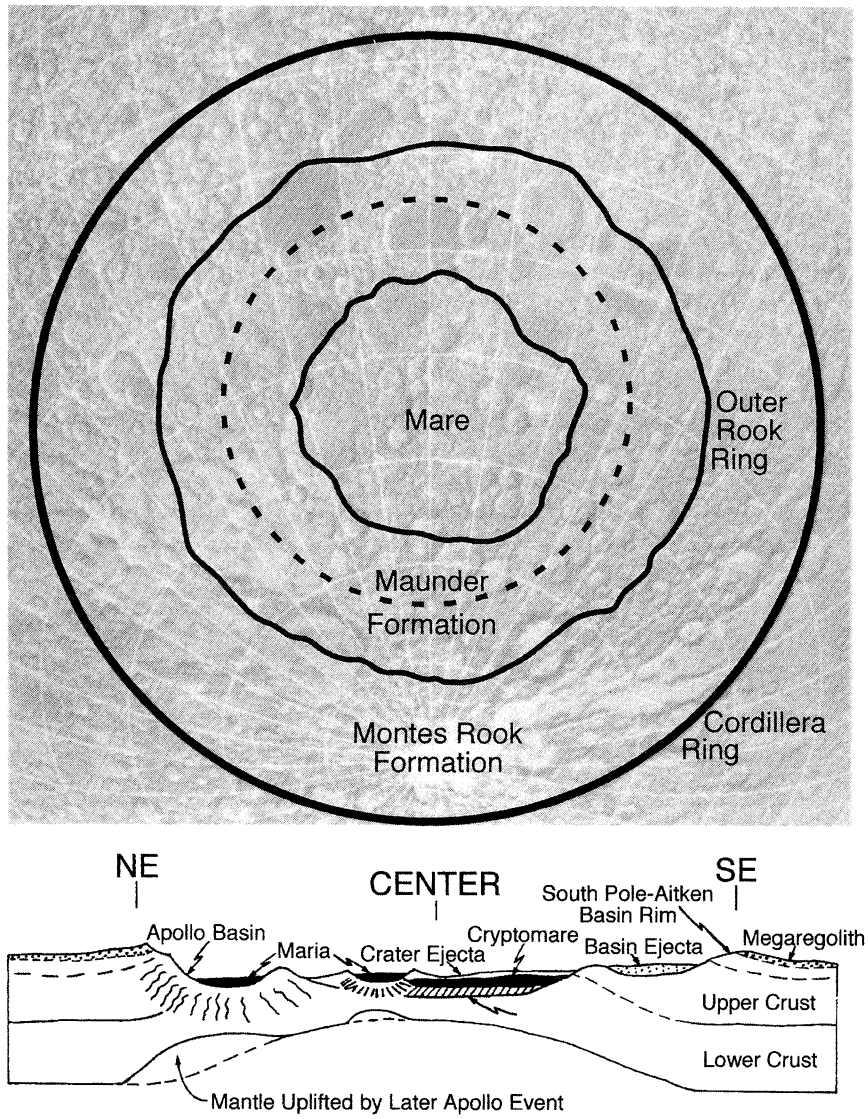

Figure 2. Inferred distribution of basin deposits within SPA on the basis of scaling from Orientale [after *Head et al.*, 1993]. As a working model, SPA diameter estimates and center positions (~56°S, 180°W) proposed by *Stuart-Alexander* [1978] and *Wilhelms et al.* [1979] are used.

they have excavated SPA floor material. For example, the Nectarian-aged Ingenii (325 km diameter) and the pre-Nectarian aged Apollo basins excavated material from the basin floor and deposited ejecta in the interior and on the rim. In the southwestern part of the basin, the 312 km diameter Early Imbrian-aged peak-ring basin Schrödinger has deposited ejecta over much of this quadrant, and has obscured two previously formed basins of comparable size [*Head et al.*, 1993]. Mare patches, predominantly Imbrian in age, were mapped on the floor of South Pole-Aitken by *Stuart-Alexander* [1978] and *Wilhelms et al.* [1979] (see summary by *Wilhelms*, [1987]. *Yingst and Head* [1997] analyzed the details of the 52 mare patches, and noted that the vast majority were located in postbasin impact structures and concentrated in low portions of the basin in areas interpreted to be thinner crust. With the new data from Galileo, *Head et al.* [1993] and *Pieters et al.* [1993] analyzed both the Orientale Basin and the South Pole-Aitken basin, providing a comparison of the youngest and oldest large multiringed basins on the Moon. They found that the exterior deposits of Orientale (the Hevelius Formation) are homogeneous spectrally, and are similar to Apollo 16 mature highland soils, suggesting an upper crustal source. The Montes Rook Formation, the annulus of basin deposits lying between the central Orientale basin and the Hevelius Formation, shows a slightly stronger mafic absorption and was interpreted to be the deepest crustal material excavated by the Orientale event. The light plains of the Maunder Formation, centrally located in the Orientale basin, are similar to the Hevelius Formation in their spectral properties, supporting interpretations from other data that they represent impact melt, a homogeneous deposit of target material dominated by upper crustal material. Mafic enhancements associated with distal Orientale ejecta deposits (e.g., in the Schiller-Schickard region) were interpreted to be cryptomaria [*Head et al.*, 1993], which erupted onto the surface in pre-Orientale times but were mixed with Orientale ejecta during the basin-forming event.

In contrast to excavation of the upper crust by Orientale, the Galileo data revealed the huge mafic anomaly on the floor of South Pole-Aitken basin [*Belton et al.*, 1992] and suggested that

the basin event excavated to deeper levels, into more mafic lower crust. No positive evidence of mantle material was found but its presence could not be ruled out [*Head et al.*, 1993; *Pieters et al.*, 1997b]. These new data and interpretations permitted a comparison between the ring-spacing and deposit distribution of the well-preserved Orientale Basin and the highly degraded South Pole-Aitken basin. Shown in Figure 2 is an extrapolation of the unit and ring positions for the Orientale basin superimposed on the South Pole-Aitken region using the SPA basin center position adopted by *Head et al.* [1993] and in this paper.

Clementine global altimetry data later confirmed both the depth and scale of SPA [*Spudis et al.*, 1994; *Zuber et al.*, 1994]. More recently, Lunar Prospector data also confirmed the enhancement of iron and slight enhancement (but variable) of thorium within the basin [e.g., *Lawrence et al.*, 1998, 2000]. The distribution of global topography of the Moon [e.g., *Smith et al.*, 1997] showed that the maximum topographic relief occurs on the farside and documented the enormous inherent size of the SPA basin (~2500 km in diameter; > 8 km deep), the largest basin on the Moon, and perhaps in the solar system [*Spudis et al.*, 1994]. These and updated gravity models provide estimates of crustal thickness [*Neumann et al.*, 1996] and suggest boundary conditions for models of crustal evolution [*Wieczorek and Phillips*, 1997, 1998, 1999; *Zhong et al.*, 1999]. As constraints on the data are better defined, these models are continually updated [e.g., *Wieczorek and Zuber*, 2001].

Armed with this plethora of background material on South Pole-Aitken basin accumulated over several decades, a number of important questions can now be posed which may be addressed with Clementine optical data. What is the detailed compositional character of South Pole-Aitken and its deposits and how do they relate to samples in our laboratories? What is the distribution of minerals and inferred rock types in the interior of the basin? What does their distribution indicate about basin size and structure? Is there evidence for the impact event excavating to lower crustal or upper mantle depths? Or was the excavation cavity relatively shallow [*Schultz*, 1997]? What is the character of the impact melt sheet and what is its distribution? How much impact melt was created and from what depth [e.g., *Cintala and Grieve*, 1998]? What is the extent of volcanism within the basin? Is there evidence for mare deposits in addition to those mapped by previous workers (e.g., ancient mare deposits or cryptomaria)? If so, what are the implications of their presence for the thermal and magmatic evolution of the basin? If samples could be returned from the floor of the basin, what sites would address the most critical outstanding questions? In this study we address several of these questions.

3. Description of Data and Data Sources

The area selected for our analysis of South Pole-Aitken basin extends from 20°S to 70°S latitude and from 140°E to -120W° (240°E) longitude. Data examined include those from the Clementine UVVIS camera and from the lidar altimeter system. All data are displayed in sinusoidal equal-area projection for ease of comparison and a 10° x 10° grid is superimposed. The 750 nm albedo mosaic for our study area is shown in Figure 3a. For reference, key features are identified in Figure 3b.

The Clementine image data were obtained by the UVVIS camera at five wavelengths: 415, 750, 900, 950, and 1000 nm. The U.S. Geological Survey (USGS) planetary image processing software (Integrated Software for Imagers and Spectrometers (ISIS) [*Eliason*, 1997; *Gaddis et al.*, 1997; *Torson and Becker*, 1997]) was used to process the raw Clementine images and produced the global Lunar Digital Image Mosaic (LDIM) [*Eliason et al.*, 1999a, 1999b] used in our analysis. Radiometric calibration and data processing steps for the LDIM included: (1) electronic offset and gain corrections, (2) dark-current subtraction, (3) nonlinearity and temperature dependent offset corrections, (4) readout or frame transfer correction, (5) flat-field and exposure-time corrections, (6) normalization to a 1 AU distance and conversion to 1 AU relative radiance, (7) conversion to reflectance, (8) photometric normalization (to standard viewing geometry of 30° phase angle, 0° emission angle, and 30° incidence angle), (9) subpixel-level coregistration to nearest 0.2 pixel, (10) projection to sinusoidal equal-area, and (11) automated mosaicking. The photometric correction is applied to permit accurate comparison of frame-to-frame reflectance values; the correction is a hybrid lunar-Lambert function involving separate corrections at different phase angle ranges [*McEwen*, 1996; *McEwen et al.*, 1998]. The data were spectrally calibrated from digital numbers (in counts/ms) to bidirectional reflectance (percent reflectance, within 5% of absolute) at the standard viewing geometry using the reflectance properties of lunar soil at the Apollo 16 landing site as ground truth to facilitate compositional analyses [*Pieters et al.*, 1997a; *Pieters*, 1999]. This procedure produces data equivalent to reflectance factor [*Hapke*, 1993], or bidirectional reflectance relative to a Lambertian surface at the same geometry.

Possible sources of error in the Clementine UVVIS data include residual calibration errors (~1% filter-to-filter [*Pieters et al.*, 1997a; *McEwen et al.*, 1998]), photometric variations within a scene, uncorrected topographic effects, scattered or stray light, and absolute radiance deviations. Residual photometric effects include wavelength-dependent variations (currently unaccounted for in the photometric normalization) at levels of ~ 0.2% across a Clementine frame and ~0.5% between frames [*McEwen et al.*, 1998; *Shkuratov and Kreslavsky*, 1998; *Hillier et al.*, 1999]. Topographic effects, particularly those due to steep slopes, change the effective geometry and can thus alter the apparent brightness of a feature [e.g., *Lucey et al.*, 1998a; *Robinson et al.*, 1999]. Scattered light is a possible cause of anomalous signal in which high-albedo units influence the measured values of low-albedo units (and vice versa) to varying degrees at different wavelengths [e.g., *Gaddis et al.*, 1995]. Similarly, stray light is a spurious component of added radiation in the image and may or may not be spatially dependent. In the Clementine data, scattered or stray light has an estimated magnitude of 8 to 12% in residual brightness near the lunar limb, and it falls to a value of ~3% at a distance of 200 pixels [*Pieters et al.*, 1994; *Li et al.*, 1999; *Robinson et al.*, 1999; *Robinson*, 2001]. Furthermore, since the spectral calibrations depend on laboratory measurements of lunar soil, the absolute radiance is also tied to the degree to which the natural surface is reproduced in the laboratory. Recent telescopic estimates of absolute lunar radiance [*Hillier et al.*, 1999; *Shkuratov et al.*, 2000] suggest the Clementine values are significantly overestimated.

Topographic information for the South Pole-Aitken basin region is derived from the Goddard Lunar Topography Model 2 (GLTM-2) [*Smith et al.*, 1997] and is shown in Figure 4. The GLTM-2, a 72nd degree and order spherical harmonic expansion of lunar radii, has a spatial resolution of 2° (~60 km), and was produced from range measurements obtained by the Clementine lidar instrument spaced at intervals of ~20 to 100 km along-track

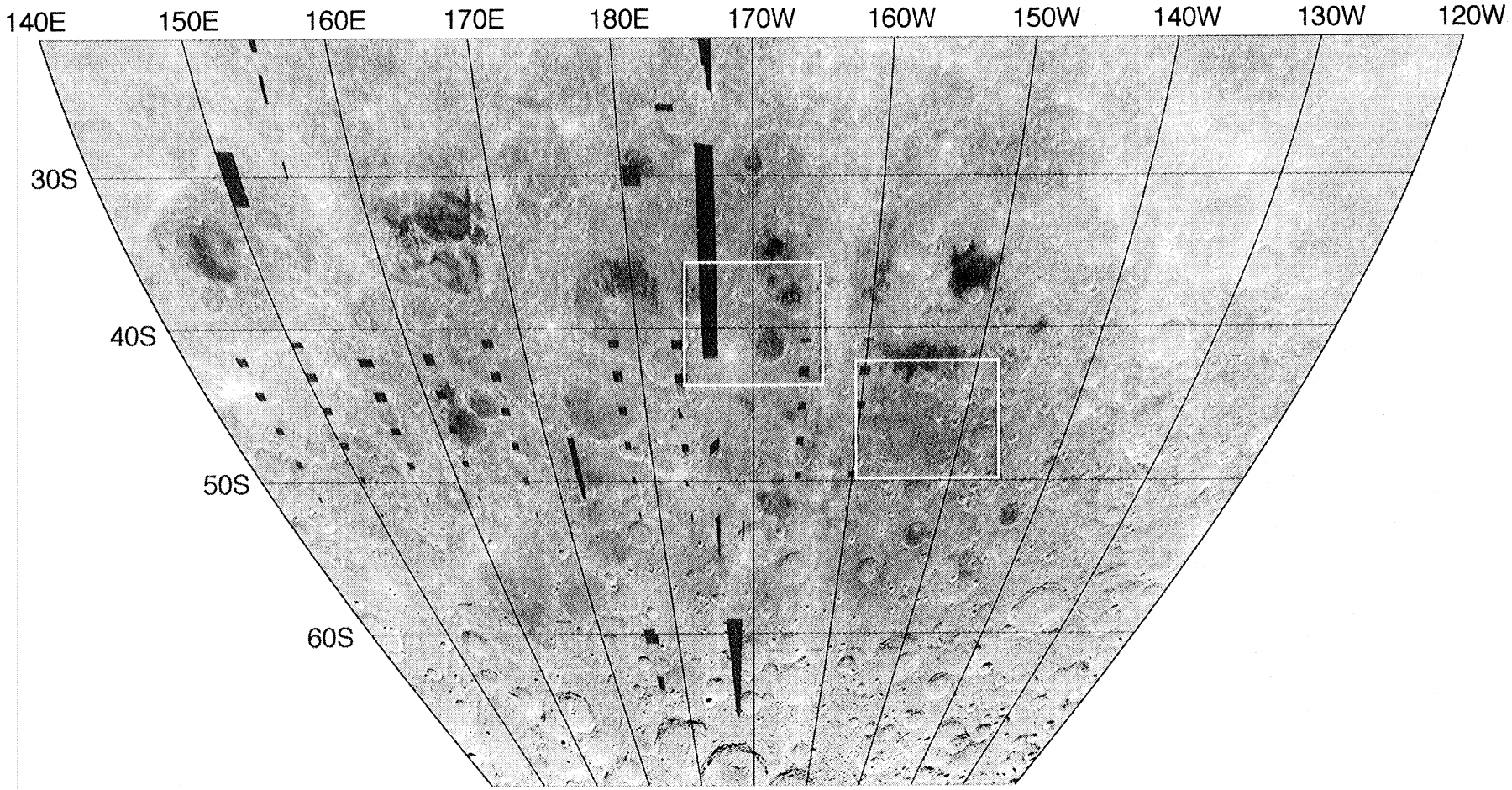

Figure 3a. SPA Clementine 750 nm albedo image mosaic for South Pole-Aitken basin sampled at 500 m/pixel. A 10°x10° grid is superimposed. This region is the basemap for subsequent figures. This view is in the Sinusoidal Equal-Area projection centered at 170°W (190°E) and extending 100° longitudinally from 220°W (140°E) to 120°W (240°E).

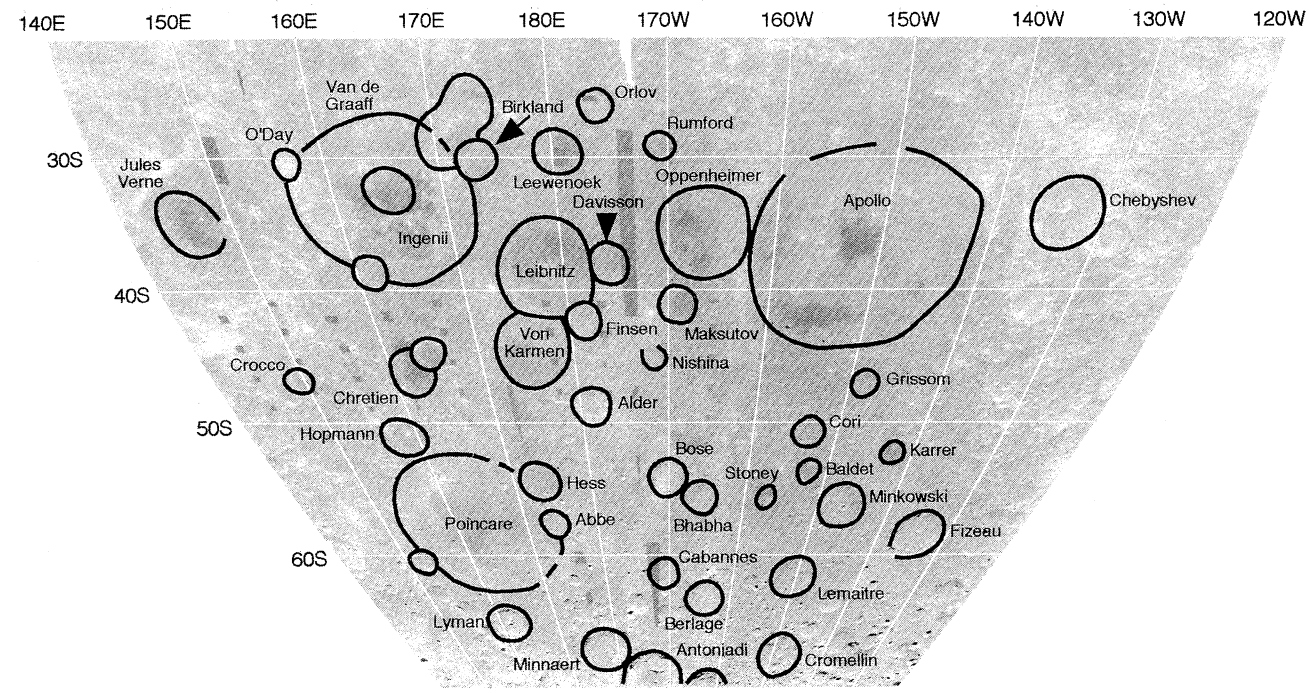

Figure 3b. Principal geomorphic features, including craters and basins within SPA.

and a maximum of 60 km across-track at the equator. Data for regions between orbital tracks were filled in with minimum-curvature interpolation. Elevations for the GLTM-2 are referenced to a spheroid with a radius of 1738 km and a dynamical flattening measure of 1/3234.93. The Clementine lidar system had an estimated radial error of ~130 m, and optimal vertical resolution of a single laser shot was 39.972 m. The absolute vertical accuracy of the GLTM-2 topography data is estimated to be ~ 100 m [*Smith et al.*, 1997].

South Pole-Aitken basin extends across several quadrangles for which geologic maps have been produced by the U.S. Geological Survey [*Scott et al.*, 1977; *Stuart-Alexander*, 1978; *Wilhelms et al.*, 1979]. Although minor discrepancies exist between map sheets at their boundaries, these maps have been

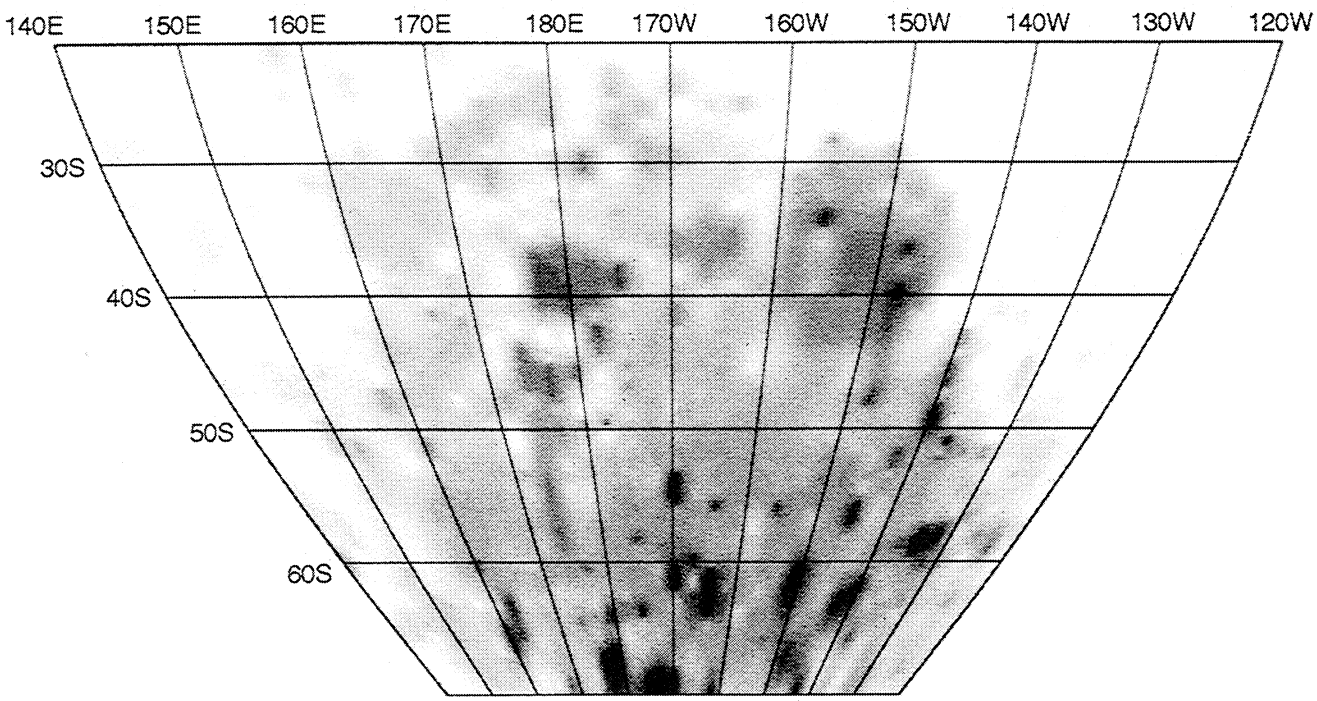

Figure 4. Topography within SPA derived from Clementine laser altimeter data [*Smith et al.*, 1997]. The data are contrast enhanced to show details of the lowest elevations within South Pole-Aitken basin.

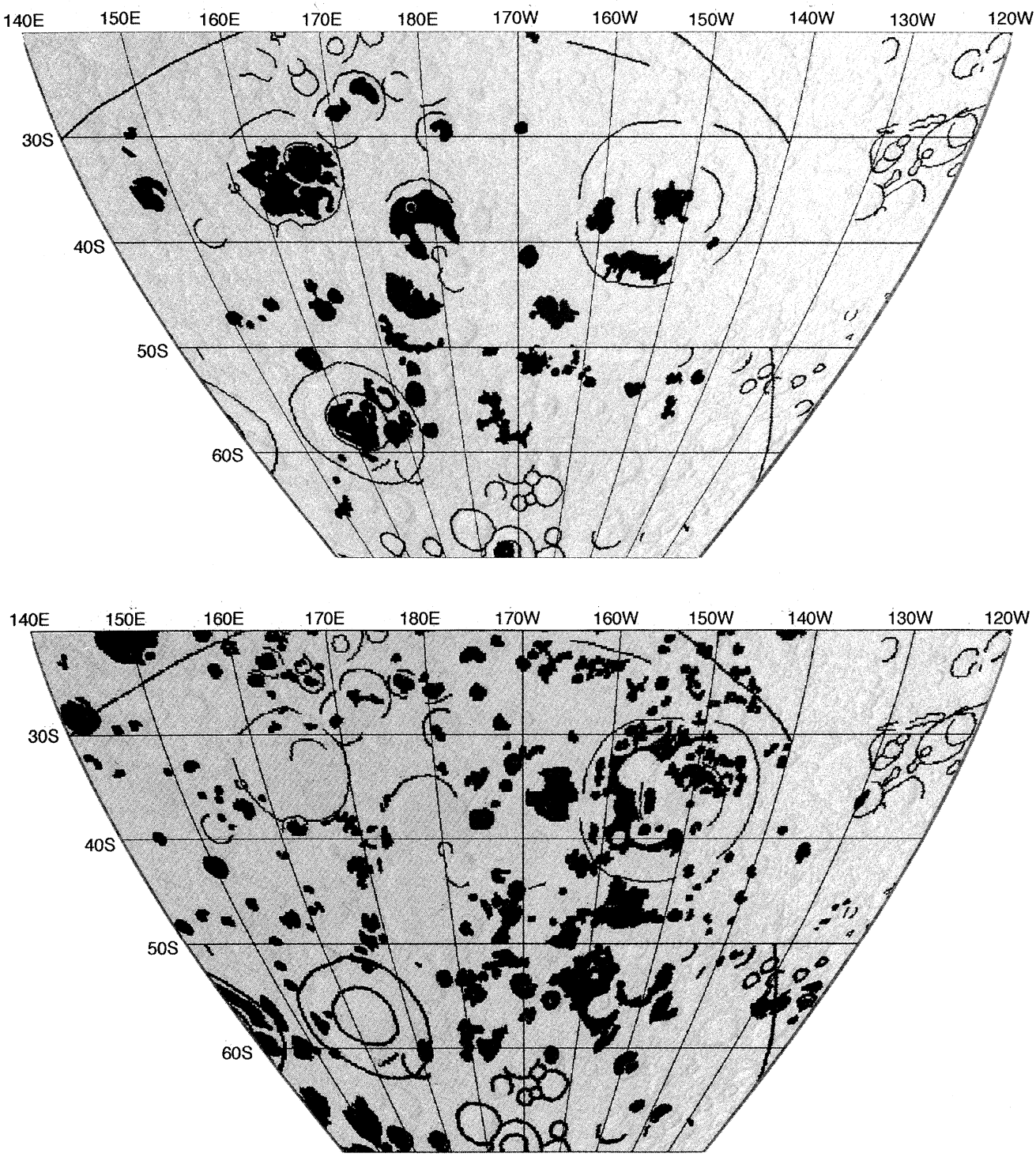

Figure 5. Sketch map showing the distribution of a) mare and b) plains units in South Pole-Aitken basin [after *Scott et al.*, 1977; *Stuart-Alexander*, 1978; *Wilhelms et al.*, 1979].

digitized and mosaicked by USGS (Flagstaff) to allow comparison of units across data sets. Sketch maps showing the distribution of the maria and smooth plains units have been abstracted from these geologic maps and are shown in Figures 5a and 5b.

4. Characterization of Rock Types

The mineralogy of lithologic units on the Moon reflects not only the composition of the material, but also the pressure and temperature conditions under which the mineral assemblage formed. The type of minerals present thus reflect important events in geologic history even though rock types of the upper crust have been brecciated and redistributed as a result of cumulative bombardment (especially during the first 500 Myr). Although many accessory minerals have been identified in the lunar samples, the minerals that constitute the bulk of lunar rocks in the Apollo and Luna collections and lunar meteorites are plagioclase feldspar (mostly anorthite), the mafic silicates

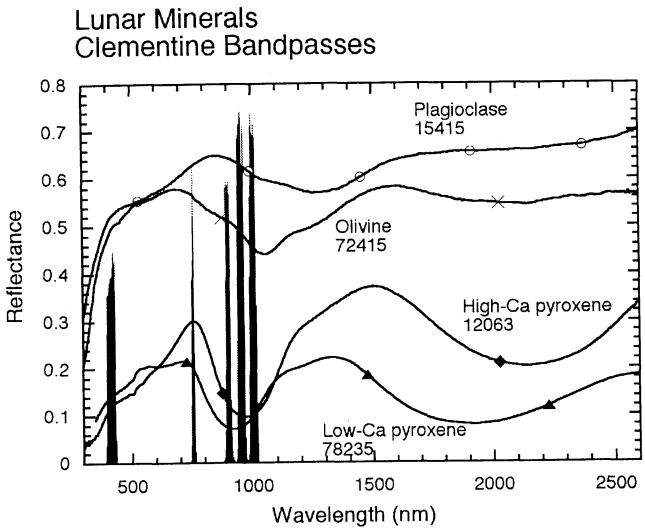

Figure 6a. Bidirectional reflectance spectra of particulate lunar minerals (i=30°, e=0°). Superimposed are the bandpasses of the Clementine UVVIS filters (arbitrary scale).

pyroxene and olivine, and Fe-Ti oxide (mostly ilmenite) [e.g., *Papike*, 1998].

The main crustal rock types of the highlands all have abundant plagioclase and have been classified by *Stoffler et al.* [1980] based largely on the proportions and types of mafic minerals present. We will use their general terminology in the discussion below. Anorthosites have fewer than 10% mafic minerals; norites are dominated by low-Ca pyroxene, gabbros by high-Ca pyroxene, and troctolites by olivine. Compositional subdivisions of highland rock types are based on the relative abundance of anorthite and each of the mafic minerals. The vast majority of returned highland samples are feldspathic noritic impact breccias. Gabbroic and troctolitic rock types are relatively rare in the sample collection. The mare basalts, which are later crustal rock types derived from partial melts of the mantle, all contain abundant high-Ca pyroxene along with plagioclase. They are subdivided into different basalt types based mainly on the abundance of ilmenite and olivine [*Papike et al.*, 1976].

Each of the mafic silicate minerals of the Moon exhibit diagnostic absorption bands in the near-infrared due to ferrous iron in the crystal structure [*Burns*, 1993]. Shown in Figure 6a are laboratory reflectance spectra of particulate samples of principal lunar silicate minerals found in lunar rocks. Superimposed on the mineral spectra are the bandpasses for the filters used by the Clementine UVVIS camera [*Nozette et al.*, 1994]. The absorptions that occur near 1000 nm for both pyroxene and olivine are due to electronic transitions within the ferrous ion. Pyroxenes also have a second ferrous band near 2000 nm. The energy (band center) and symmetry of these absorptions are controlled by the structure of the particular mineral and thus are highly diagnostic of mineral composition.

Note that for the ferrous absorptions observed near 1000 nm, low-Ca pyroxenes exhibit a relatively short wavelength absorption (near 930 nm), high-Ca pyroxenes exhibit a longer wavelength absorption (near 980 nm), and olivines exhibit a multiple band with a band minimum beyond the range of Clementine UVVIS filters (near 1050 nm). When one of these mafic minerals plus plagioclase dominates a rock type exposed on the lunar surface, the Clementine bandpasses are well situated to distinguish among the three. The primary distinction summarized above can be seen readily in Figure 6b where the mineral spectra have been resampled with the Clementine bandpasses for the 750, 900, and 1000 nm filters.

A very important consideration in any analysis of remote sensing data for the Moon is the degree to which the properties of surface materials represent (1) unaltered rock types (which can be compared directly to familiar compositions of returned samples) or (2) "weathered" materials (whose properties have been highly altered in the space environment). Particulate samples of a rock carry the diagnostic spectral signatures of constituent minerals [*Adams and McCord*, 1971a, 1971b] and are well suited for mineral identification. The rubble surrounding a fresh impact crater or exposed along steep slopes represents immature samples from which we infer local mineralogy. Much effort has been directed toward understanding the details of processes acting on lunar materials exposed on the surface and their effects on optical properties (see discussion and references in *Pieters et al.* [2000] and *Lucey et al.* [2000b]). Returned samples of well-developed regolith formed on distinct geologic units exhibit properties that are quite different from those of the local predominant lithology [e.g., *Heiken et al.*, 1991; *Pieters*, 1993]. For the characterization of rock types using spectroscopic data, the most important property is that absorption bands of mature lunar soils are substantially weakened compared to those of a particulate sample of local rocks. Furthermore, in order to discern the critical diagnostic shape of these weaker absorptions, it is necessary to remove an additional continuum slope developed during the weathering process.

Although limited in spectral range, the five-channel Clementine UVVIS data can be used to estimate the strength of ferrous absorption near 1 μm and hence can detect and characterize relatively fresh (unweathered) particulate ferrous material on the surface. Since these 5 channels do not cover the long wavelength wing of the absorption, however, the data cannot provide information on the shape of weak absorptions in well-developed, or mature, regolith. For our characterization of materials within South Pole-Aitken basin we concentrate on the localized areas that have not accumulated substantial weathering products (such as at fresh craters or steeply sloped topography). These areas provide the best assessment of local mineralogy.

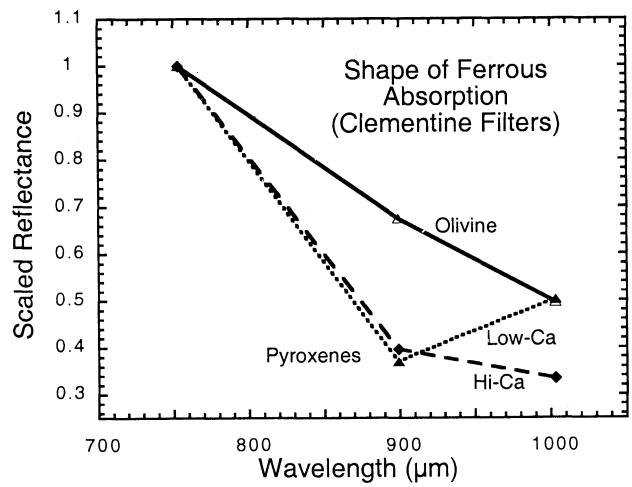

Figure 6b. Spectra of the mafic minerals in Figure 6a resampled with the Clementine 750, 900, and 1000 nm filter bandpasses and scaled to unity at 750 nm.

To characterize the rock types in and around South Pole-Aitken using Clementine data, two approaches are used. The first (the albedo+band-depth, or the "Hawaii method") is used to distinguish anorthosites (low FeO) from rock types with significant mafic minerals (high FeO). This was first presented by *Lucey et al.* [1995] and later refined by *Blewett et al.* [1997] and *Lucey et al.* [1998a, 2000a]. The second approach (band-shape, or the "Brown method") is used to distinguish among the different mafic-bearing rock types based on the mineralogy of freshly exposed surfaces. This method has its roots in the approach of *Tompkins and Pieters* [1999] and is presented for the first time here.

4.1. Albedo + Band Depth

Two optical parameters, albedo and band strength for the ferrous absorptions, are very sensitive to the presence and abundance of mafic minerals. For lunar rock types the abundance of plagioclase and mafic minerals vary inversely, as is evident in the extremely high inverse correlation observed between Al_2O_3 content and FeO for lunar samples [e.g., *Heiken et al.*, 1991]. Exposure to the space environment both reduces the albedo and weakens the band strength. These compositional and space weathering relations are illustrated in a scatterplot of the optical parameters albedo (at 750 nm) and band strength (approximated by the ratio 1000/750 nm), such as the scatterplot derived from Clementine data for much of SPA shown in Figure 7. Throughout this analysis, we use the 1000/750 nm ratio instead of the 950/750 nm ratio used by Lucey and collaborators because the 1000 nm band appears to be less susceptible to calibration errors. The 950 nm band is often associated with spurious errors of unknown origin [see *Staid and Pieters*, 2000], which are most prominent in deep shadows.

The breakthrough concept formulated by *Lucey et al.* [1995] recognized a general relation between these two optical parameters: low-Fe anorthositic materials border the data cloud across the top (little or no ferrous absorption over a range of albedo), whereas iron-rich mafic-rich materials border the data cloud along the left (low albedo and a range of band strength). Mature soils fall in the dense upper left portion of the data cloud. In the context of these two optical parameters, a rotational mixing relation (that pivots around a hypothetical common value for low albedo, weak band) is defined by Lucey et al. which captures much of the variation in FeO between low-iron, high albedo materials and high-iron, low albedo materials. The rotational position of any data point between these two regimes provides an estimate of its iron abundance [*Lucey et al.*, 1995]. Lunar samples are used to provide an empirical calibration, the most recent of which is described by *Lucey et al.* [2000a]. A valuable trait of this empirical formulation associating optical parameters with composition is that it is relatively insensitive to many of the effects of space weathering [*Lucey et al.*, 2000b]. The approach thus provides a mechanism to map estimates of FeO across the Moon in a spatial context. Although it is less appropriate for distinguishing among the high iron maria [*Staid and Pieters*, 2000] or glass-rich pyroclastic material [*Gaddis et al.*, 2000; *Lucey et al.*, 1998a], the approach is an excellent technique to map bulk properties of many lunar soils. In the discussion below, we use the most recent calibration for Clementine data [*Lucey et al.*, 2000a] to map regions associated with SPA that appear to be highly anorthositic (low-iron).

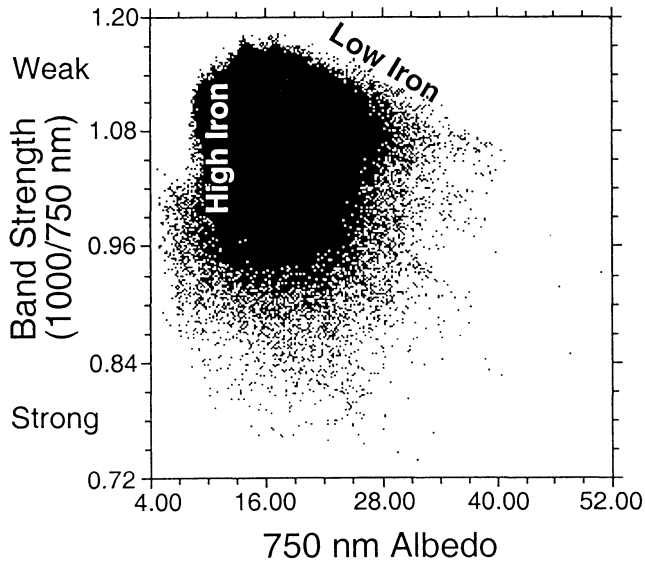

Figure 7. Scatterplot of SPA data comparing albedo (750 nm reflectance) and an estimate of band depth (1000/750 nm) values. These two optical parameters include low-iron materials along the top and high-iron materials along the left side. A rotational mixing relation between the two (calibrated to lunar samples) can be used to estimate FeO abundance [*Lucey et al.*, 1995; *Lucey et al.*, 2000a].

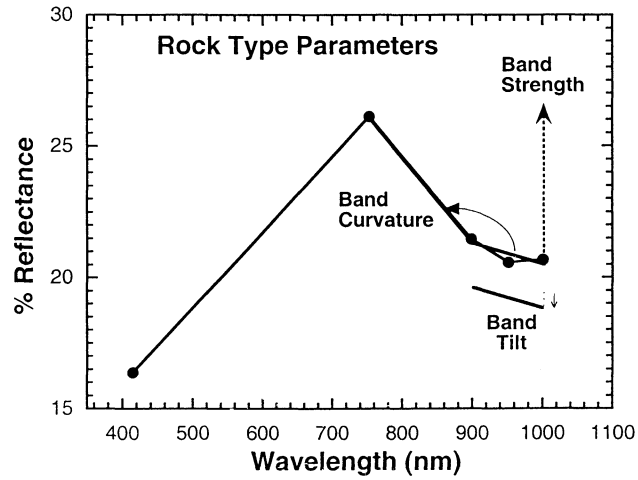

Figure 8. Schematic diagram of the three optical parameters used here to characterize the type of mafic mineral present using Clementine UVVIS five-channel data.

4.2. Band Shape

The original approach developed by Tompkins to distinguish between different mafic-bearing lithologies used two optical parameters to characterize the diagnostic shape of the ferrous band near 1000 nm: band strength (called "key ratio") and band curvature [*Tompkins and Pieters*, 1999]. In order to easily map the distribution of different lithologic units using the two-dimensional data of Clementine color mosaics, we have expanded this scheme to include a third parameter, band tilt. The relationship of these three parameters for Clementine UVVIS five-channel data are shown in Figure 8. With these three optical parameters, the rock types across SPA can be readily evaluated using RGB color-coding.

Band strength is approximated by a ratio of the intensity within the ferrous absorption to that outside the band at shorter wavelengths on the continuum; we use the ratio 1000/750 nm. Areas with a weak band (anorthosites as well as mature soils) have a high value in this parameter; areas with a strong ferrous band (without extensively weathered soils) have a low value. In subsequent color composites this parameter is assigned to the blue channel. Unweathered areas with abundant mafic minerals exposed will thus not be significantly blue. Anorthosite would appear deep blue in this parameterization, and well-developed soils all have a significant blue component.

Band curvature is an angular measurement (in radians) between the reflectance values of 750 to 900 to 1000 nm. Units are arbitrary (dependent on the wavelength and reflectance unit used), but areas with a high curvature have low numerical values in this parameter and relatively strong mafic absorption bands and areas with no curvature or weak mafic bands (a linear spectrum over this wavelength range) have higher numerical values in this parameter. Thus areas with abundant low-Ca pyroxene (noritic) would have a high curvature, areas with abundant high-Ca pyroxene would have lower curvature, and olivine-rich areas would have very little curvature. In subsequent color composites this parameter is assigned to the red channel (assigned inversely by value). Areas with abundant low-Ca pyroxene exposed would thus appear red.

Band tilt is measured by the difference in reflectance at 900 and 1000 nm. Unlike band curvature, band tilt has little dependence on band strength. Band tilt is thus less susceptible to minor residual errors in phase corrections between 750 nm and the longer wavelength bands in the near-infrared (e.g., 900, 950, 1000 nm). For unweathered areas with immature, freshly exposed material (such as at young craters), band tilt and band curvature are approximately complementary. For example, a strong ferrous band with almost no curvature, such as a high-Ca pyroxene or an olivine, would usually exhibit large values of tilt (reflectance at 900 nm is greater that that at 1000 nm). In subsequent color composites this parameter is assigned to the green channel. Areas with abundant high-Ca pyroxene and/or olivine would appear green. Note that this parameter alone does not distinguish between high-Ca pyroxene and olivine.

Examples of SPA five-color Clementine spectra that demonstrate the key variations of these three band shape parameters are shown in Figure 9, and the inferred local rock types the spectra represent are summarized in Table 1. The band shape analysis is best suited for distinguishing among rock types at optically immature surfaces containing different amounts of various mafic minerals. Anorthosites can be identified in this scheme (by the lack of ferrous band), but as discussed in section 4.1 albedo information is also necessary to distinguish anorthositic material from general soils. In the discussion below, our selected color code for the three band shape parameters emphasizes mapping relatively fresh unweathered mafic lithologies. Anorthosite and anorthositic materials are mapped and discussed separately, but combined in a general rock-type image.

These mafic rock type identifications necessarily refer only to the dominant type of mafic mineral present based on good approximations of band shape. For these lithologies, no attempt has been made to quantify the relative abundance of mafic mineral relative to plagioclase, although such estimates are our overall goal. In order to analyze absorption band characteristics in a more quantitative manner, the continuum on both sides of the 1000 nm ferrous band must be known. It is anticipated this next

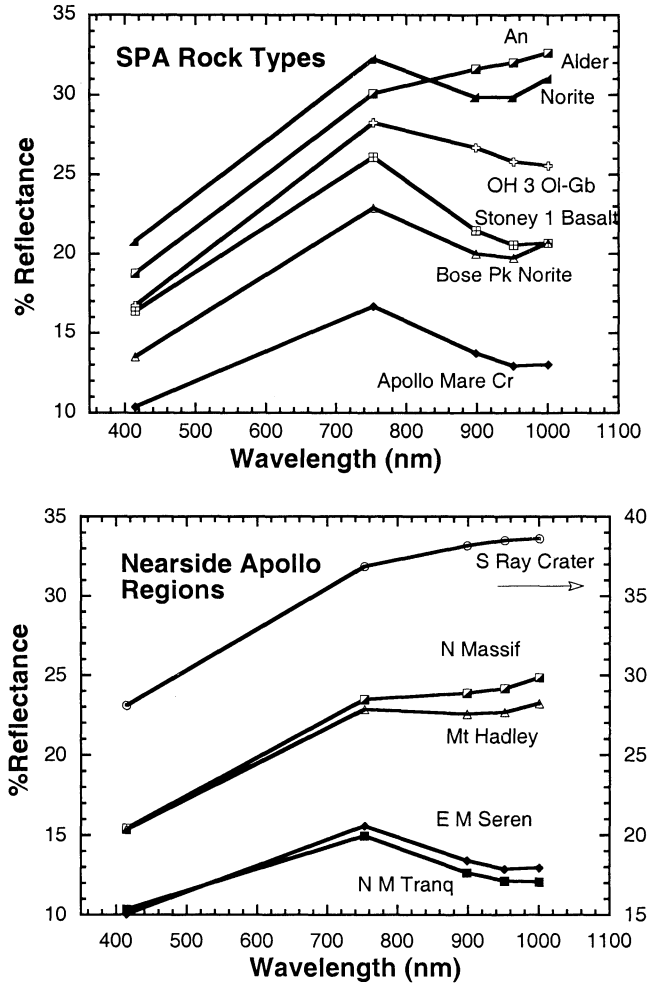

Figure 9. Representative 5-color Clementine spectra for a) different rock types observed in South Pole-Aitken and b) regions near Apollo sampling sites.

level of analysis may be possible [e.g., *Le Mouelic et al.*, 2000] when the near-infrared Clementine data are calibrated and processed [*Lucey et al.*, 1998b] or when data from new orbital near-infrared spectrometers are available [*Otake et al.*, 1997].

For comparison, Clementine spectra in and around Apollo landing sites generally exhibit less prominent absorption features than spectra from SPA. None of the regions containing Apollo landing sites were near large fresh craters with abundant unweathered mafic rocks. Shown in Figure 9b are representative five-color spectra for features that might represent immature surfaces near Apollo sites. All highland features exhibit properties of weakly noritic breccias (anorthosite to noritic anorthosite): Mount Hadley (Apollo 15), South Ray Crater (Apollo 16), and South Massif (Apollo 17). On the other hand, nearby mare craters in Mare Serenitatis (MS) and Mare Tranquillitatis (MT) exhibit the classic characteristics of basalts containing abundant high-Ca pyroxene. Comparable information on the three spectral parameters used for rock type identification are provided in Table 1 for these near-side areas.

Note that with this general characterization of mafic rock types based on spectral parameters sensitive to ferrous absorptions, no direct distinction can be made on the basis of grain size, ie., between relatively fine-grained basalt (extrusive volcanism) and coarse-grained gabbro (intrusive). Both are

Table 1. Clementine Rock Type Parameters for Representative Regions in SPA and Near Apollo Landing Sites

Site	Band Strength 750/1000 nm	Band Curvature 750-900-1000 nm	Band Tilt 900-1000nm	Rock Type (General)	Color in Plate 1
Alder S rim A 50°S, 178.3°W	weak	none	up	anorthosite	deep blue
Alder S rim N 49.8°S, 177.7°W	med. Strong	high	up	norite	red/orange
Olivine Hill 3 57.7°S, 163.9°W	strong	none	down	ol-gabbro	green/yellow
Stoney 1 52.5°S, 157.8°W	strong	med. Low	down	basalt/gabbro	yellow/green
Bose W peak 54.1°S, 169.3°W	med. Strong	high	up	norite	red
Apollo Basin mare 35.6°S, 150.3°W	strong	med. Low	down	basalt	green/yellow
S Ray Crater 9.1°S, 15.4°E	weak	none	up	anorthosite	[blue]
N Massif [a] 21.3°N, 30.7°E	med. Weak	medium	up	noritic anorthosite	[orange/purple]
Mt Hadley [a] 26.5°N, 4.2°E	med. Weak	medium	up	noritic anorthosite	[orange]
E M Seren. Cr [a] 19.7°N, 24.4°E	strong	med. Low	down	basalt	[yellow/orange]
N M Tranq. Cr [a] 14.5°N, 27.8°E	strong	med. Low	down	basalt	[green/yellow]

[a] The "Color" for the nearside areas are from images comparable to Plate 1.

identified by the presence of abundant high-Ca pyroxene. In the discussion below, we will normally refer to a mineral assemblage that contains abundant high-Ca pyroxene as gabbroic, regardless whether its origin is plutonic or volcanic. In addition, if the surface morphology of a nonmare unit is smooth and low-lying (i.e., mapped as smooth plains), but also contains local features (craters) that indicate the presence of abundant high-Ca pyroxene, we feel confident in identifying the underlying unit exposed by the craters as mare basalt and classify it as cryptomare.

5. Distribution of Feldspathic Materials

The distribution of feldspathic materials across the SPA study area is shown in Figure 10. The areas mapped are those with < 6% FeO using the FeO algorithm of *Lucey et al.* [2000a]. These areas thus include anorthosites along with feldspathic soils no more iron-rich than those of Apollo 16. From this map it is seen that anorthositic material clearly rings the central part of the SPA study area. Although almost the entire interior of the study area is significantly more iron-rich, extensive or gradational deposits of

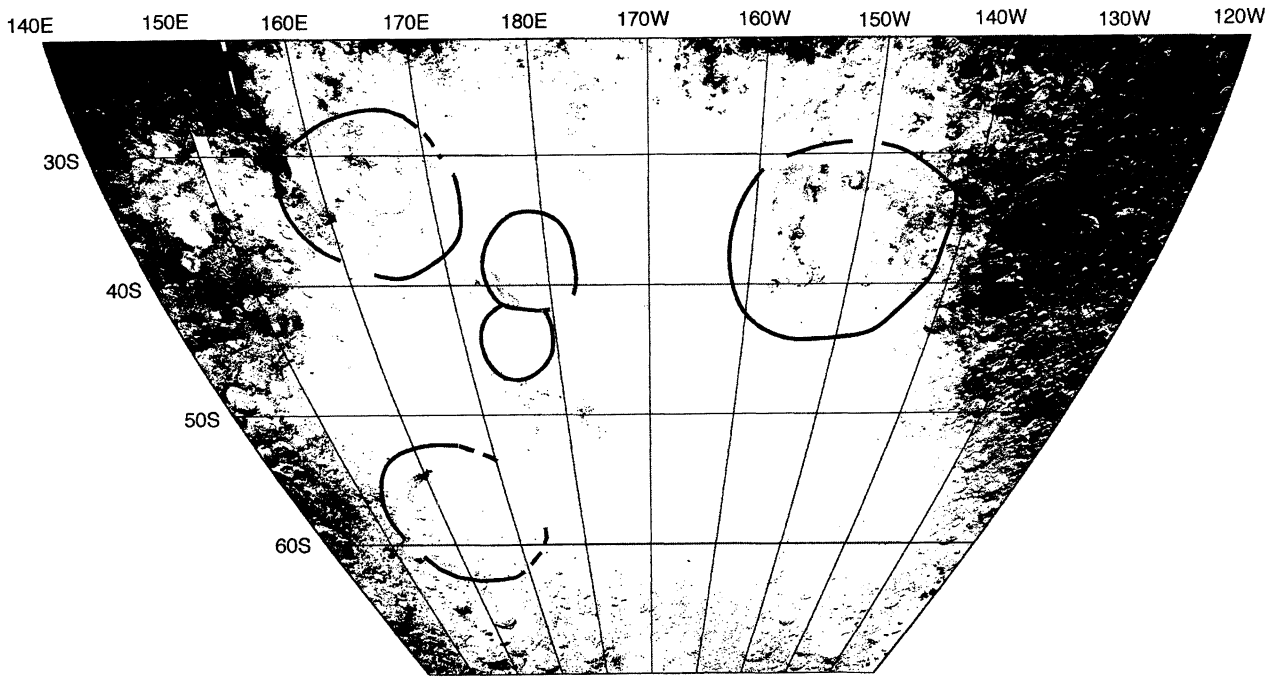

Figure 10. Distribution of anorthositic regions. Areas identified as <6% FeO [*Lucey et al.*, 2000a] are indicated as filled pixels on the basemap grid. (Pixels with values less than negative 2% FeO were eliminated as spurious.)

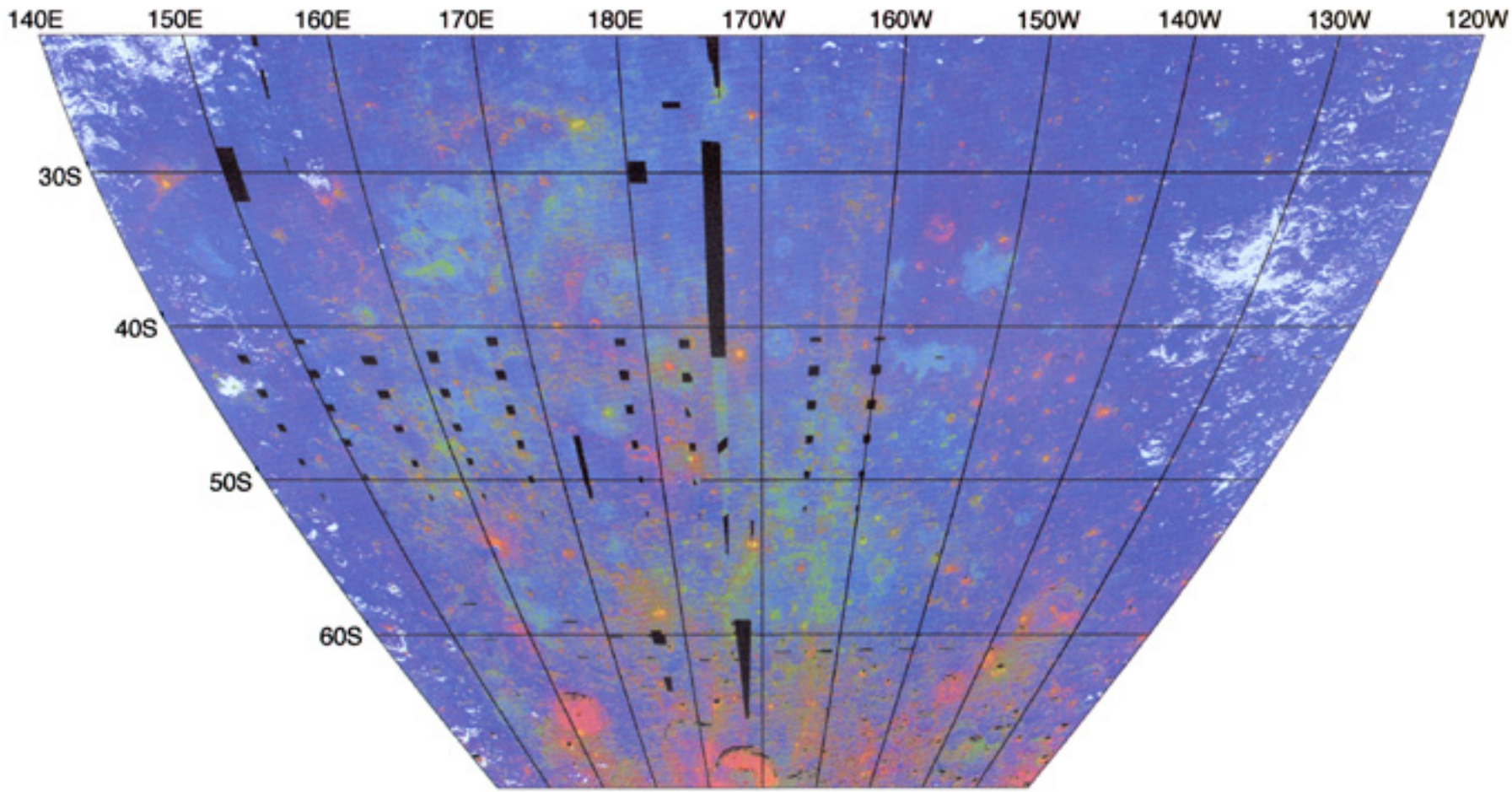

Plate 1. Rock types of South Pole-Aitken basin for the same region as in Figures 2-4. The color composite image was produced using Clementine 500 m data. RGB color display assignments are R, band curvature^{-1}; G, band tilt; and B, band strength. As described in the text and summarized in Table 1, the pervasive blue coloration indicates regions with well developed mature and/or anorthositic soils (weak bands), red and orange areas contain abundant noritic components, and yellow and green tones indicate the presence of abundant gabbroic (basaltic) or olivine-rich lithologies. Anorthosites (estimated <3% FeO [*Lucey et al.*, 2000a]) are shown in ice blue. Data gaps and deep shadows are shown in black.

mafic-bearing material are not seen exterior to this region. Note that for latitudes below ~60°S, geometry effects may bias the estimates toward lower iron abundance for some bright sunlit-facing walls of craters. In comparison to the earlier Galileo analyses, these higher-resolution Clementine data show much more clearly that the area interpreted to be exterior to the basin cavity (e.g., outside the Outer-Rook ring equivalent, see Figure 2) is notably feldspathic. This is in good agreement with the global analysis comparing Clementine and Lunar Prospector data [*S. D. Chevrel et al.*, 2000]. These Clementine data also suggest the presence of small, but well-defined, localized regions of anorthositic material that occur in areas that could be interpreted to be within the cavity itself (e.g. in the peak-ring and Maunder Formation equivalents of Figure 2).

5.1. Apollo and Ingenii

Both of these basins are ancient and occurred within SPA in pre-Nectarian times after the SPA event [*Wilhelms*, 1987]. Both are near the edge of SPA and both exhibit anorthositic materials in their interior (e.g., the inner ring of Apollo, the rim of Thomson). Anorthosite in the ring of Apollo has been documented in previous analyses [*Morrison and Bussey*, 1997; *Morrison*, 1998]. These anorthosite-bearing rings are surrounded by the more mafic-rich materials common to SPA, and both basins were later partially filled with mare basalt. Nevertheless, the occurrence of anorthositic material throughout these rings suggests that the original SPA melt sheet or breccia deposits in these regions were underlain by relatively anorthositic crustal material and that the SPA deposits were sufficiently thin to allow the underlying anorthositic material to be uplifted to form the peak rings in Apollo and Ingenii.

5.2. West Central SPA

The eastern part of the central SPA study area is devoid of any anorthositic material, but the western part of the central study area exhibits two NW trending zones of material identified as anorthositic. These appear to be associated with a few large pre-Nectarian craters, Leibnitz (245 km diameter; ~38°S, 179°E) and von Karman (180 km diameter; ~45°S, 176°E), both of which were also later filled with mare materials. The anorthosites occur along somewhat elevated ridges (see Figure 4). Upon closer inspection, the anorthosite at Leibnitz appears as high-albedo small 1-5 km knobs along the SW rim. These often neighbor more mafic-rich knobs. The regions along the southern edge of von Karman are more spatially diffuse and intermediate in albedo. The character and origin of these centrally located anorthosites are discussed further in section 10.2.

6. SPA Mafic Rock Types

Using the Clementine band shape parameters described above, an overview of the rock types across the South Pole-Aitken basin study area is shown in the color composite of Plate 1. The expansive blue-toned areas in the NE and NW part of the study area are indicative of the relatively feldspathic character of regions representing the ejecta and megaregolith exterior to the basin after SPA formation. In this color composite, areas estimated to be <3% FeO by the *Lucey et al.* [2000a] method are shown separately in ice blue. The interior of the SPA study area exhibits extensive Fe-bearing lithologies. The overall mineralogical character of the mafic-rich interior is identified by abundant exposures of rocks and breccias of noritic composition

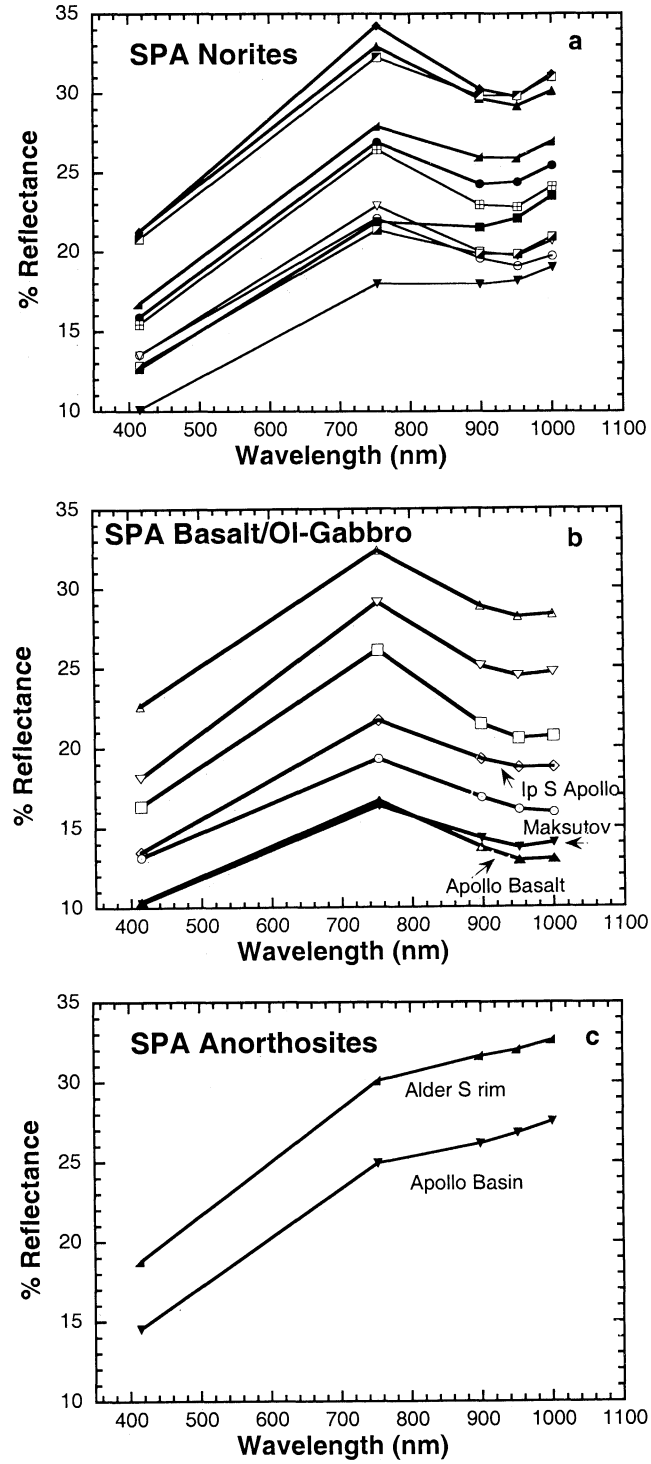

Figure 11. Clementine five-channel reflectance spectra of the principal rock types within SPA: (a) norites, (b) basalts, and gabbros, and (c) anorthosites.

(red and orange tones), but a wide range of mineralogical diversity occurs locally and regionally (numerous isolated yellow and green areas). Figures with sections of Plate 1 that provide close-up examples of the distinction between mafic lithologies are presented and discussed separately below.

Validation of the qualitative information in the two-dimensional color composite of spectral parameters shown in Plate 1 is provided by five-color spectra that were extracted from

the Clementine mosaics for several areas representing a wide range of red/orange, green/yellow, and deep blue regions. Spectra for the principal rock types have been grouped according the general rock type they represent in Figure 11 and are discussed in sections 7 and 8. More atypical regions are discussed in section 9.

1. Norites. These areas have a short wavelength ferrous absorption indicating low-Ca pyroxene is the dominant mafic mineral present. Noritic materials are pervasive across the much of the study area and appear red/orange in Plate 1.

2.) Basalts and gabbros. These areas have a longer wavelength ferrous band with little curvature indicating that high-Ca pyroxene is the dominant mafic minerals present. Fresh craters in basalt units appear yellow to green in Plate 1. One example (the darkest spectrum, squares in Figure 11b) is for a crater in a mapped mare deposit on the floor of Apollo basin; another is for a crater in the mare filling Maksutov. All other spectra are from candidate areas of ancient maria. They are small craters that either occur on smooth plains or on the floor or rim of a nearby larger crater.

3) Anorthositic materials. Although rare within SPA, anorthositic material with no detectable ferrous minerals is identified at a few sites (most readily seen in Figure 10; see section 5).

6.1. Maksutov and Oppenheimer

The areas of previously mapped maria [*Stuart-Alexander*, 1978; *Wilhelms et al.*, 1979; *Yingst and Head*, 1997] (Figure 5a) of Imbrian age are low albedo and appear light green to blue (or turquoise) in Plate 1. The turquoise color, linked to the low albedo of these soils through the tilt parameter, does not provide direct mineralogical information. As expected, however, small craters within these maria expose fresher basaltic material rich in high-Ca pyroxene and appear green to yellow. A closer look at one of these areas is provided in Figure 12a and Plate 2a to show these relationships. Maksutov (83 km diameter; ~42°S, 169°W) is mapped as a lower-Imbrian age crater filled with Imbrian age mare [*Stuart-Alexander*, 1978; *Wilhelms et al.*, 1979]. To the north is the larger Nectarian age crater Oppenheimer (208 km diameter) which contains abundant pyroclastic deposits [*Gaddis et al.*, 2000; *Head et al.*, 2000; *Petro et al.*, 2001]. Excluding the blue-tone mature soils across the region (and part of an orbit with calibration difficulties in the lower left), all the exposed rock types in this region are noritic (red/orange-tone), except for the small basaltic craters in the mare within Maksutov, which appear green. A particularly noteworthy compositional contrast is the equally small noritic central peaks (red/orange) that protrude above the basalt. Furthermore, the low albedo pyroclastic deposits in Oppenheimer to the north exhibit no mineral signatures that would indicate the presence of crystalline basalt at local small craters, thus implying that these dark deposits are a form of glass or crystallized beads, similar in form (but probably not composition) to those of Apollo 17 [*Weitz et al.*, 1999].

6.2. Plains South of Apollo

Shown in Figure 12b and Plate 2b is an area of smooth, light-plains south of the Apollo basin that has clearly been modified by Orientale ejecta from the east [*Stuart-Alexander*, 1978; *Wilhelms et al.*, 1979]. Apollo basalts can be seen at the top of the image and exhibit the characteristic properties of mare basalt (with small green craters indicating the presence of high-Ca pyroxene). The heavily cratered terrain along the eastern edge of the image is dominated by noritic rock types (orange/red) and this lithology appears to extend discontinuously around the smooth plains. In contrast, the craters within the smooth plains, many of which may be secondaries from Orientale, have exposed material with a distinctly gabbroic composition, namely abundant high-Ca pyroxene (green). We thus interpret these smooth plains to be pre-Orientale ancient basalts that have been overlain by thin deposits of non-mare material. This scenario is similar to that envisioned for a region east and southeast of the Orientale Basin [*Head et al.*, 1993; *Mustard and Head*, 1996], in which mare volcanism began before the Orientale event. The emplacement of feldspathic ejecta accompanying the Orientale event mixed with the surface mare deposits, producing cryptomaria with the appearance of smooth plains. The mapping of secondary craters from Orientale across these SPA smooth plains [*Wilhelms et al.*, 1979] further supports this cryptomare interpretation.

The nonmare deposits, which mask the older mare here, may themselves predate the Orientale event. Orientale secondary craters have excavated through these surficial deposits exposing basaltic material. Thus, the deposits appear to have occurred prior to the craters. In addition, the albedo of soils developed on these "smooth plains" deposits south of Apollo is too low to simply be a mixture of basaltic mare and the feldspathic Orientale debris when compared to cryptomaria on the eastern side of Orientale on the nearside. These SPA deposits overlying ancient mare would be more consistent with local derivation. Altogether, these ancient maria in SPA may indeed be a relatively early episode of lunar basaltic volcanism and are certainly older than basalts represented by the Apollo and Luna collections.

7. Distribution of Basaltic Volcanism

Several of the 52 mare deposits previously mapped within SPA [*Stuart-Alexander*, 1978; *Wilhelms et al.*, 1979; *Yingst and Head*, 1999] were analyzed by *Yingst and Head* [1999] using Clementine data. They found that 19 of 21 deposits analyzed could be confidently identified as maria, and that some of these appear to have been contaminated by lateral and vertical mixing from subjacent and nearby noritic material. In our analyses, each of the mapped maria of Imbrian or Eratosthenian age shown in Figure 5a was investigated with the rock type classification discussed above. The mineralogy observed at fresh craters was emphasized, but the boundaries of individual maria were not assessed in detail. With only a few exceptions (discussed below), all mapped maria have low albedo and they exhibit the distinct signature of high-Ca pyroxene at fresh craters, similar to that observed at Maksutov (Figure 12a; Plate 2a). These features confirm a basaltic composition. All mapped mare deposits that have been confirmed to have basaltic composition are indicated as solid regions in Figure 13. Clementine data for a few small mapped areas are inconclusive, and these areas are not included.

A few of the mapped mare deposits are regionally dark at 750 nm but significant parts of the region do not exhibit evidence for the presence of pyroxene (i.e., they lack prominent ferrous absorption) at local small craters. Although the five-channel Clementine data cannot uniquely characterize these materials, their appearance and their optical signature would be more consistent with the presence of pyroclastic materials, possibly mixed with or overprinted by local (less mafic) material [e.g., *Weitz et al.*, 1998; *Gaddis et al.*, 2000]. These areas generally fall into the Group 1 classification of *Gaddis et al.* [2000]. We have identified several places where pyroclastic volcanic material probably exists within SPA based on low albedo with weak or

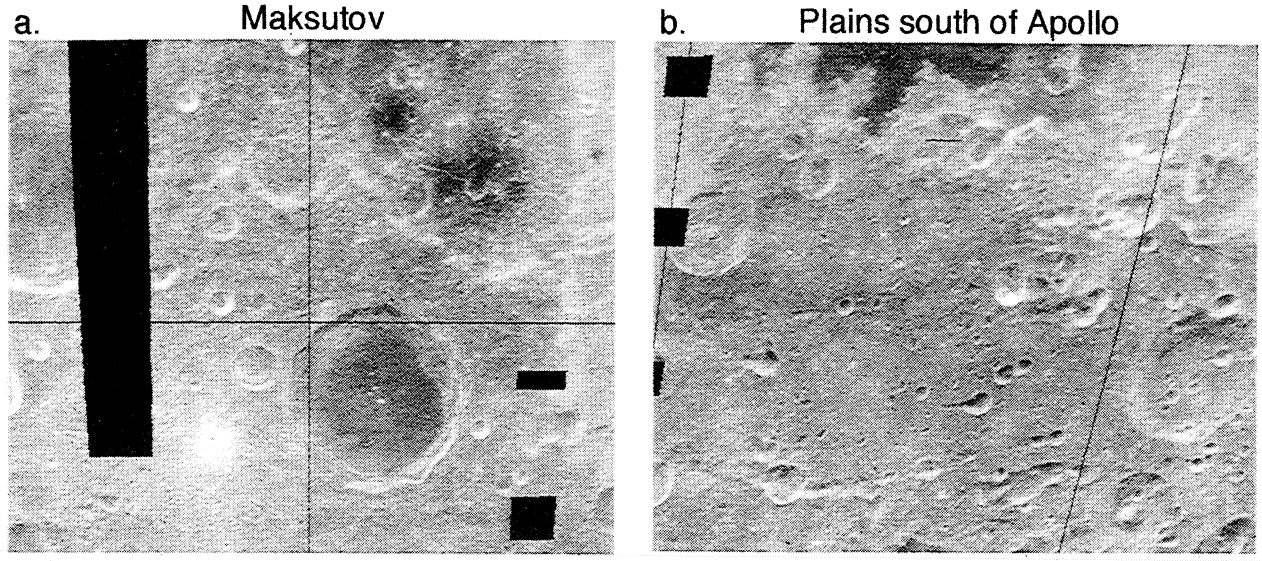

Figure 12. Albedo images (750 nm) for the areas in Plate 2: (a) Maksutov and Oppenheimer and (b) Plains south of Apollo.

nonexistent ferrous absorption and these are indicated as stippled areas in Figure 13.

An initial evaluation of the mapped areas of smooth plains (Figure 5b) was also undertaken. These areas generally have a higher albedo and crater density than the mapped maria and predate Orientale. A small number of the larger regions clearly exhibit a basaltic signature at fresh craters, similar to the smooth plains south of Apollo discussed above, but many regions of smooth plains do not. In addition, a large number of the mapped smooth plains regions are small and these Clementine data are inadequate to provide a reliable assessment of their mineral composition. Included in Figure 13 are those areas of smooth plains which we interpret to be inherently basaltic based on the detection of high-Ca pyroxene at fresh craters within the unit. These areas would generally be called cryptomaria [e.g., *Head and Wilson*, 1992; *Head et al.*, 1993]. We conclude that basaltic

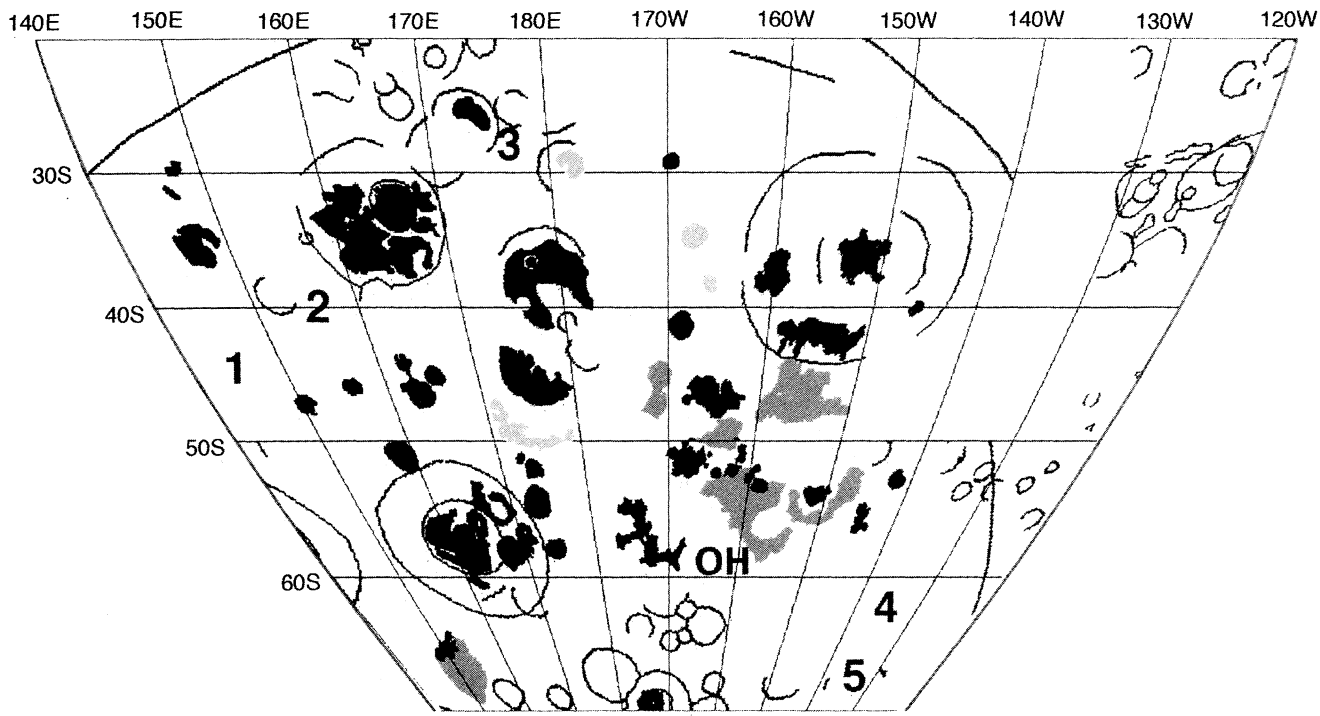

Figure 13. Distribution of known and likely mare basalts within SPA. Mapped maria (figure 5a) that are confirmed to be basaltic are indicated as solid areas. Mapped maria that are likely pyroclastic deposits are indicated as light gray; Oppenheimer pyroclastics are also included. Smooth plains (Figure 5b) that are intrinsically basaltic are indicated as dark gray. Gabbroic or olivine-rich areas that are not topographically smooth are indicated by 1, 2, 3, 4, 5, and OH (see text for discussion).

volcanism was an ongoing process in the pre-Orientale period of SPA evolution as well as in the Late Imbrian period of mare volcanism.

8. Distribution of Norite

The striking signature of mafic materials in SPA seen in the color composite of Plate 1 is clearly of a noritic composition, after regions of known or suspected mare basalt composition (Figure 13) are eliminated. The presence of abundant low-Ca pyroxene (red tones in Plate 1 and Plate 2) is pervasive across the SPA study area. This mineralogy is not associated with one region or one size of crater (i.e., depth of penetration). It is seen to occur in all environments from craters as small as a few km to rims, ridges, and central peaks of some of the largest craters. The extensive distribution of noritic compositions vividly illustrated in Plate 1 verifies the original detection of noritic materials dominating SPA by *Pieters et al.* [1997b], which was later confirmed by *Blewett et al.* [2000].

This pervasive nature of norite within SPA suggests a first-order conclusion about its origin. Most, if not all, of this noritic material must represent some form of the principal impact debris and/or impact melt created during the SPA basin-forming event. It is not necessarily homogeneous, but the dominant mafic mineral is low-Ca pyroxene, either as a primary mineral or as the principal mafic component of a crystallized melt. This material forms a deposit about 1500 km across in the central part of the study area (Plate 1), which is located primarily within the central part of the basin interior as interpreted from topography and the extrapolation of deposits and ring structure from the Orientale Basin (see Figure 2). The location of these SPA noritic deposits is analogous to the area inside the Orientale Outer Rook Ring, within which is located the Maunder Formation, interpreted to be dominated by impact melt deposits (see discussion by *Head et al.* [1993]). In the case of Orientale the melt sheet is derived largely from upper crustal material, while in SPA, the melt sheet is derived largely from lower crustal material.

9. Other Gabbroic Areas

Examination of Plate 1 allows several localized gabbroic mafic areas to be identified that are neither noritic nor mare basalt. These regions are associated with a single crater located in generally more heavily cratered terrain than mare and smooth plains, but the crater and deposits nevertheless exhibit characteristics of a long wavelength ferrous band (high-Ca pryoxene or olivine). The location of six such mafic non-mare regions are indicated in Figure 13.

9.1. Nonmare Gabbroic Regions

Areas 1, 2, 3, 4, and 5 are associated with impact craters (area 1: 43°S, 144°E; area 2: 39°S, 157°E; area 3: 26°S, 176°E; area 4: 62°S, 137°W; area 5: 67°S, 135°W). Representative 5-color Clementine spectra for these regions are shown in Figure 14. In geologic maps [*Scott et al.*, 1977; *Stuart-Alexander*, 1978; *Wilhelms et al.*, 1979], areas 1, 2, 4, and 5 are all unnamed Eratosthenian or Imbrian aged craters. Area 2 is the region identified by *Blewett et al.* [1999] as an unnamed dark haloed crater. Area 3 is an unmarked area on the edge of van de Graaff that appears to be a fresh crater.

The very fresh unnamed crater (area 1) located along the western edge of the SPA study region has excavated anorthosite (spectrum SPA-G1An), which is offscale in Figure 14a (top), is

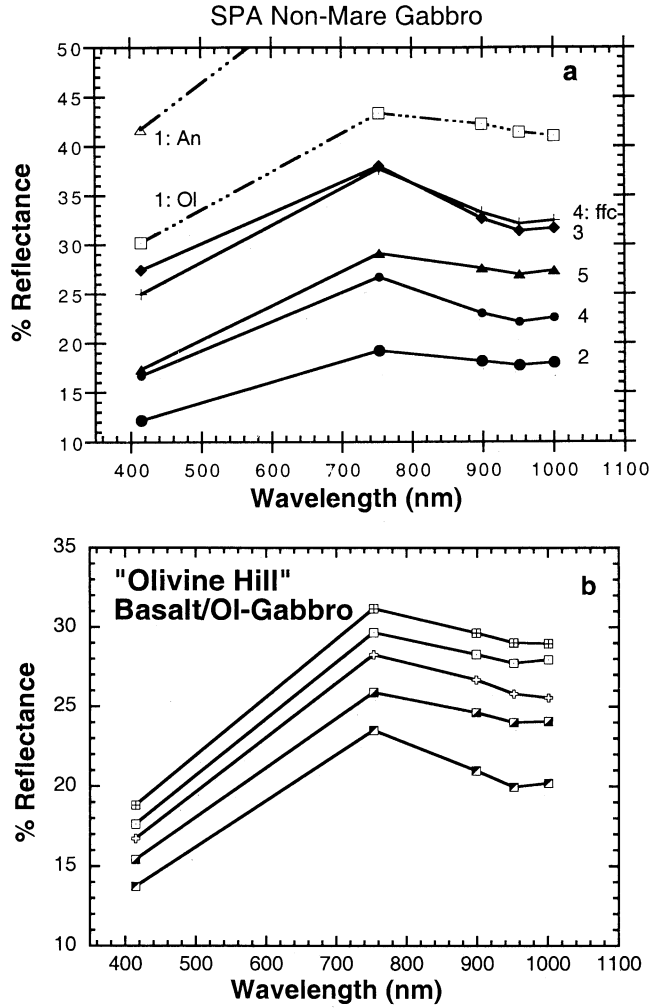

Figure 14. Clementine five-channel reflectance spectra for gabbroic (non-mare basalt) regions within SPA. a) Regions exhibiting high-Ca pyroxene or olivine associated with a single crater. The coordinates for these areas are centered on: 1 (43°S, 144°E), 2 (39°S, 157°E), 3 (26°S, 176°E), 4 (62°S, 137°W), 5 (67°S, 135°W). (b) Olivine Hill region (a broad region near 57°S, 160°W).

bright, and exhibits no ferrous absorption. Area 1 also appears to contain abundant olivine-dominated material (spectrum SPA-G1Ol). The dominant lithology at Area 1 is thus almost certainly troctolite. On the other hand, based on observed spectral characteristics Areas 2, 3, 4, and 5 all contain various amounts of high-Ca pyroxene as the principal mafic mineral, although some amount of olivine cannot be precluded.

These areas, and perhaps others not yet identified, merit detailed study. There are several possibilities for their origin, including: (1) mafic plutons formed during crustal formation, (2) mafic components of a localized (possibly differentiated) melt sheet, (3) ancient mare basalt that has been extensively covered by subsequent debris, (4) stalled dikes or sills of basaltic composition, (5) fragments of lower crust or mantle brought near the surface during SPA formation.

9.2. Olivine Hill (OH)

One nonmare region that exhibits a notably long-wavelength ferrous absorption is not associated with a single crater, but

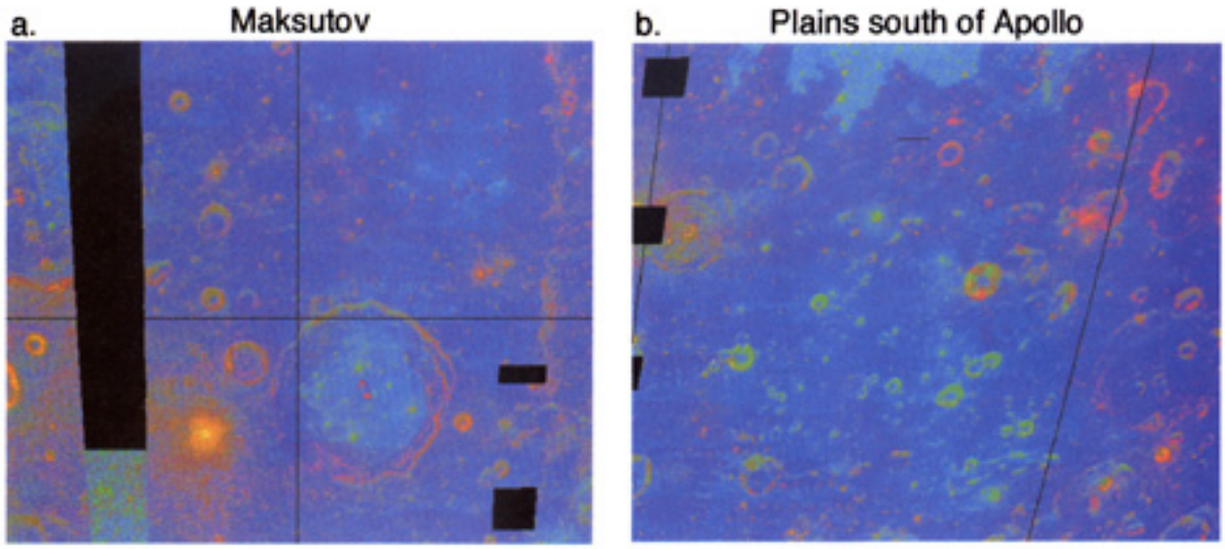

Plate 2. Subsections of the rock type map of Plate 1: (a) Maksutov and Openheimer and (b) Plains south of Apollo.

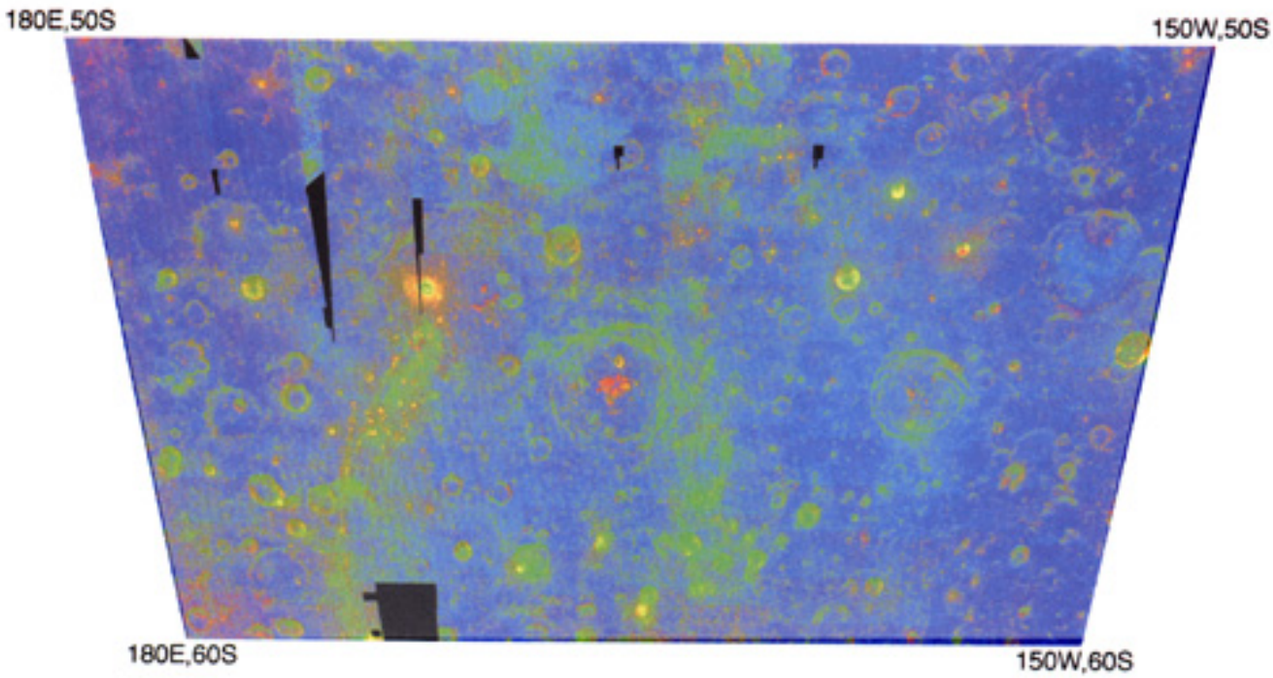

Plate 3. Rock types of central SPA from the full-resolution Clementine data sampled at 100 m/pixel. The region extends from 180°W to 150°W and 50°S to 60°S. The same RGB color composite assignments as Plate 1 is used with the same stretches.

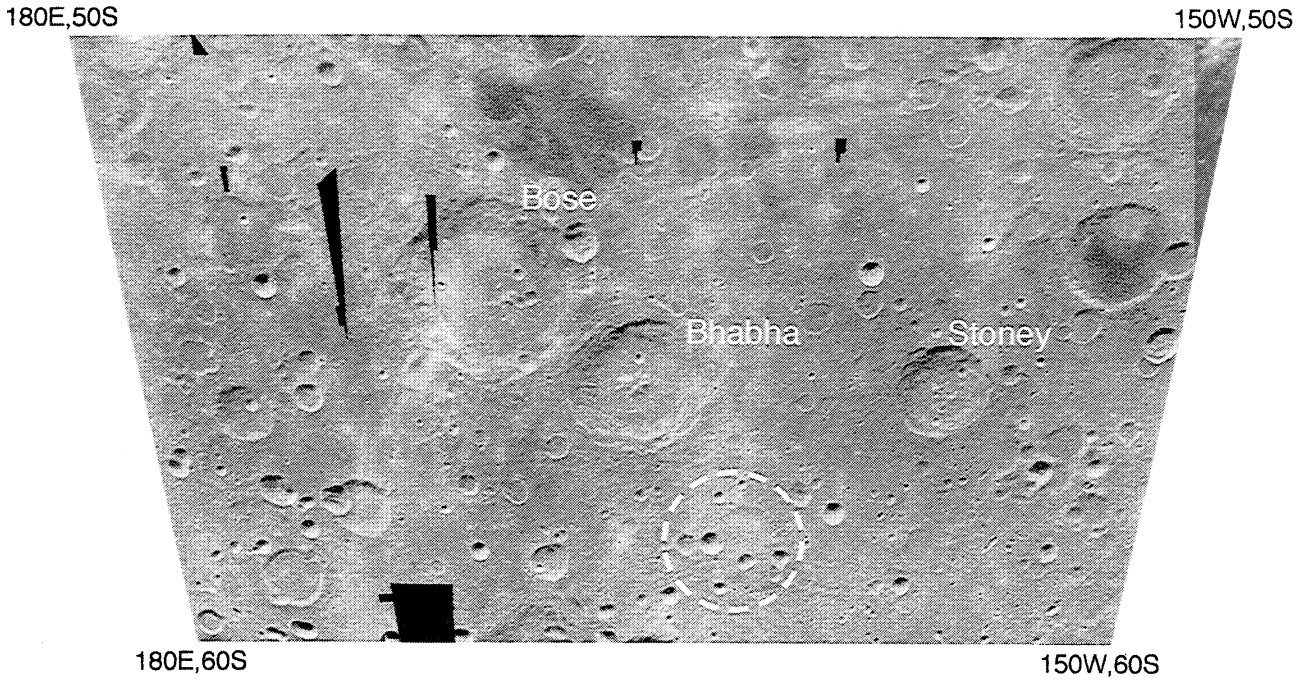

Figure 15. Albedo image (750 nm) for the central SPA area. The data are from the full resolution Clementine data sampled at 100m/pixel. The region extends from 180°W to 150°W and 50°S to 60°S. The location of Olivine Hill is indicated with a discontinuous circle. (See Plate 3 for the distribution of rock types.)

covers a rather large region centered near 57°S, 160°W [*Pieters et al.*, 2001]. Except for the probable troctolite at Area 1, spectra from this area exhibit the longest wavelength ferrous absorption observed in the SPA region, suggesting abundant olivine may be present. Their five-color spectra suggest an overall mineralogy of olivine-gabbro. Topographically (Figure 4) this area is slightly elevated above typical surroundings, even though it is essentially in the center of the basin, and we thus call the region "Olivine Hill" (OH). The slightly elevated topography of this region (750 m) was independently confirmed by the digital elevation model of *Cook et al.* [2000]. Other evidence for its relatively high topography comes from embayment relations between plains, which show that this region has a slightly higher crater density and albedo compared to surrounding lower-albedo, smoother deposits, suggesting that it was topographically high and escaped burial during subsequent mare flooding. Spectra for several fresh craters in this OH region are shown in Figure 14b.

To examine this general region in more detail, the central portion of SPA basin is shown at higher resolution in Figure 15 and Plate 3. The "Olivine Hill" region of olivine-bearing gabbro is indicated by a dashed circle in Figure 15. These images are derived from the highest resolution Clementine data (at 100 m/pixel) and have the same assignments and stretches as those of Figure 3a and Plate 1. The region has experienced a complex history. The crater in the center of the image (with bright red central peaks) is the crater Bhabha (64 km diameter; 55.1°S 164.5°W); northeast of Bhabha is the crater Bose (91 km diameter; 53.5°S 170.0°W). Mare basalts and basaltic smooth plains occur at various places along the top of the image and to the southeast of Bose.

The stratigraphic relations between the diverse materials observed in this region are not immediately obvious. The central peaks of both Bhabha and Bose have clearly excavated noritic material from depth. The walls and floors of both of these large craters exhibit blocks of both noritic and gabbroic compositions. A few general scenarios that are consistent with the data and merit detailed study include the following possibilities for the origin of the olivine-gabbro at Olivine Hill:

1. Uplifted upper mantle. The SPA noritic melt sheet is thin in this region. Bhabha and Bose have excavated basement noritic lower crust. The Olivine Hill region is a small zone of uplifted olivine-rich gabbroic lower crust or upper mantle, some of which is included in the walls of Bhabha.

2. Pooled mantle-derived impact melt/breccia. Bhabha and Bose have excavated components of a noritic lower crust (either as a melt sheet/breccia or as basement). The character of the slightly uplifted SPA melt sheet/breccia that resides in the center of the basin at Olivine Hill, however, tapped a deeper layer of crust/mantle and is substantially enriched in olivine compared to the pervasive noritic deposits elsewhere. The slight elevated nature of the region occurred not long after or contemporaneous with the basin. Although homogeneous elsewhere, the SPA melt sheet was not well mixed radially from the center to the rim.

3. Foreign deposits from surrounding basins. The olivine-gabbro at Olivine Hill is foreign to SPA and represents a deposit from a distal crater event. This scenario is perhaps least likely because no abundant mafic-rich materials have been observed in association with any subsequent basin-forming events.

4. Cryptomare. Olivine-rich volcanism. The unusual mafic materials at Olivine Hill are a unique type of volcanism not seen elsewhere in SPA. The elevated nature of the region argues against this scenario unless a later mechanism for uplift can be found after emplacement.

10. Interpretations and Conclusions

10.1. Basaltic Volcanism

Mare volcanism fills many of the large craters and basins within SPA basin [*Stuart-Alexander*, 1978; *Wilhelms et al.*, 1979; *Yingst and Head*, 1997; 1999]. The style of volcanism has been

shown to include both mare basalt as well as pyroclastic deposits. We have confidently identified several areas of Imbrian-aged plains that appear to represent cryptomaria, modified by mixing of ejecta from the Orientale Basin event. This clarifies earlier proposals [e.g., *Head et al.*, 1993] that cryptomaria might contribute to the broad mafic anomaly seen in the SPA interior [*Belton et al.*, 1992]. Basaltic volcanism has thus occurred in SPA from pre-Orientale to Late Imbrian periods. The SPA cryptomaria deposits are thin as is evidenced by the abundant outcrops of norite in nearby areas and the nonmare signatures of some large craters in these areas. Our assessment of basaltic volcanism in SPA increases earlier estimates of area and volume of mare deposits that were emplaced within SPA basin [*Yingst and Head*, 1997, 1999], but the volumes still fall far short of those typical of the nearside basins [e.g., *Head and Wilson*, 1992].

10.2. SPA Anorthositic Materials

Apollo and Ingenii postdate SPA, and the anorthositic material found across these two smaller basins likely represents crustal material displaced during their formation. This implies not only that the overlying mafic-rich debris from SPA was thin, but also that at least some anorthositic upper crust remained after the formation of SPA at these locations. We interpret these regions to represent the SPA collapsed basin rim, which could be comparable to the Montes Rook Formation of Orientale. Reference to Figure 2 shows that Apollo and Ingenii fall on the boundary between the equivalent of Montes Rook Formation (interpreted to be outside the basin and dominated by basin ejecta) and the equivalent of the Maunder Formation (interpreted to be inside the basin and dominated by impact melt). Inspection of the interpreted cross-section for SPA (Figure 2) shows that upper crustal material is predicted to be exposed in the zone equivalent to the Maunder Formation area due to listric faulting of the basin rim [e.g., *Head et al.*, 1993] and that it may indeed be directly exposed in the massifs forming the Apollo and Ingenii rings.

The two NWW-trending bands of apparent anorthositic material observed in the western central SPA study area are more difficult to interpret. The pervasive mafic rich SPA debris across the entire central basin must have been formed from an extensive mafic-rich zone. This in turn implies a relatively deep source region from below the anorthositic upper crust. The minor amount of anorthositic material in central SPA study area can be consistent with several descriptions of the basin and its history:

1. If the NWW-trending bands of anorthositic material have a similar origin to the anorthosites observed at Apollo (uplifted blocks of upper crustal material), then the western part of central SPA cannot have provided the mafic material seen in the relatively homogeneous SPA noritic impact debris. The deepest part of the transient cavity would therefore need to be confined to a rather small zone to the east in the eastern central SPA.

2. If the transient cavity tapped lower crust/mantle to form the mafic-rich debris and did indeed encompass much of central SPA, then some mechanism must be found to displace very large blocks (perhaps up to 300 km in extent) of anorthositic crustal material during the SPA basin forming event. This might be accomplished by listric faulting of the basin rim and lateral translation of material inward toward the basin. These outcrops could represent structures that may be the toes of the listric faults.

3. Some of the areas identified as very feldspathic from spectral parameters (Figure 10) may not be classified correctly. Because of the very weak ferrous band of some pyroclastic material, extensive pyroclastic deposits mixed with higher albedo material may be masquerading as a region of low-iron material, specifically along the southern edge of von Karman. This alternate interpretation is consistent with the nearby location of potential pyroclastic deposits associated with the regional mare. If this option is the case, then centrally located SPA anorthosites are actually found only at SW Leibnitz and at the crater Alder. In both cases the anorthosite outcrops occur as small 1-10 km sized blocks interspersed with more mafic blocks or deposits.

4. Some of the feldspathic areas could be remnants of the upper parts of a differentiated melt sheet [e.g., *Cintala and Grieve*, 1998]. The small amount of anorthosite observed at Alder, for example, may represent such a local differentiated body (there may also be mafic materials other than norite in the eastern walls of this crater). However, the pervasive occurrence of noritic compositions to considerable depths (craters of all sizes) in non-mare areas of SPA argues against extensive differentiation of the primary impact melt/breccia (see below). Alternatively, if the anorthosite is buoyant relative to the SPA melt sheet, perhaps large blocks have been transported as melt migrated in the terminal stage of the event.

10.3. Character of SPA Excavated Materials

The lack of significant feldspar-rich rocks within the SPA study area is good evidence that the upper crust has largely been stripped away by the SPA basin-forming event. The pervasive nature of noritic compositions observed across the basin indicates that this noritic lithology represents the bulk composition of the excavated material, which may occur in the form of impact melt or breccia. We cannot readily distinguish impact melt from exposed basement lower crust at local areas within SPA using data currently available, even if such a noritic composition is the dominant rock type of the lower crust. Both crystallized impact melt and lower crust basement or debris would exhibit a similar noritic mineralogy and composition. The scale and relative homogeneity of the SPA noritic units, nevertheless, argue against a ubiquitous differentiated impact melt. Small craters, walls of large craters, steep mountains, and central peaks uplifted from depth all exhibit the same noritic composition across the entire basin. This lack of variation among features that have sampled different depths strongly suggests the bulk of the melt sheet did not undergo significant differentiation.

Of great interest are those local and regional nonmare areas that deviate from this pervasive noritic composition. Several areas can be identified that exhibit properties suggestive of significant high-Ca pyroxene and/or olivine. Further investigation may resolve whether these areas represent remnants of a melt sheet of a more mafic composition, uplifted deep crust or mantle, local differentiated melt sheet, post-SPA intrusions (plutons or stalled dikes), or something else. The compositional structure within SPA is complex and reflects multiple competing processes active on the early Moon.

10.4. Possible Implications for Basin Structure

There is a suggestion that the actual center of the SPA basin occurs more to the east of that previously proposed (~56°S, 180°W) by *Stuart-Alexander* [1978] and *Wilhelms et al.* [1979] (e.g. Figure 2). On the basis of (1) the distribution of the deepest SPA topography not directly associated with other craters (Figure 4), (2) the distribution of feldspathic material, which suggests shallow crustal deposits within the basin (Figure 10), and (3) the distribution of noritic melt breccia within the basin (Plate 1), the

possibility that the actual center of the excavation cavity may have been up to 15° farther to the east, near Olivine Hill, is a reasonable working model. Such a tentative identification of a more eastern SPA center appears consistent with our current data, but requires additional geophysical constraints for substantiation.

10.5. Possible Targets for Sample Return

This initial evaluation of the rock types in South Pole-Aitken basin illuminates but does not resolve several of the outstanding questions concerning the early evolution of the Moon, and of the farside in particular. The rock type assessment does, however, provide a useful framework with which to initiate further research. High on the list of priorities is sample return from this most unusual lunar terrain. A likely sampling strategy would be to sample the initial SPA impact melt/breccia and to determine whether materials from deeper in the crust or mantle are either included in the breccias or exposed elsewhere. On the basis of our assessment of the rock types across SPA, an initial list of several possible areas include:

1. Olivine Hill. This anomalous region could represent the long-sought deep seated material from the lower crust and/or mantle (uplifted material or crystallized deep impact melt). A site should be selected to obtain samples of the olivine-gabbro as well as some of the pervasive noritic lithology which is believed to represent the impact melt/breccia.

2. Bose borehole. The small crater in western Bose has clearly exhumed diverse materials onto an already diverse floor of a large crater. The concentric rings (olivine-gabbro-norite) of materials appear to indicate the ~7 km crater tapped a gabbroic and possibly olivine-rich zone from below a more noritic upper zone. The nearby central peaks are believed to represent materials from the noritic lower crust.

3. Bhabha peaks. These notably noritic central peaks must certainly represent the principal melt sheet or uplifted lower crust of SPA. There is sufficient diversity along the floor and walls to expect samples of additional, perhaps deeper, stratigraphic units.

11. Summary

The above presentation and discussion of the rock types observed within South Pole-Aitken basin has led to several very important conclusions about the nature of the basin. These interpretations provide potential constraints about the earliest history of the lunar farside.

The anorthosite upper crust has been effectively removed across almost all of South Pole-Aitken basin. Remnants of the original feldspathic crust can only be seen in the peak rings of subsequent peripheral basins.

The melt sheet/breccia filling the basin is uniformly noritic in composition and accounts for most of the mafic anomaly seen in Clementine and Lunar Prospector data. We interpret this mafic SPA melt sheet to represent the bulk composition of the lower crust (perhaps with small amounts of upper mantle). The homogeneity of the SPA melt sheet at all scales suggests to us that it has not differentiated as a whole.

The period of basaltic volcanism within South Pole-Aitken basin includes several episodes that extend over several hundred My (pre-Orientale to Late Imbrian). The scale or volume of volcanism within SPA, however, did not reach those observed for the nearside.

An anomalous slightly elevated region near the center of the basin (Olivine Hill) exhibits a notably olivine-rich composition and currently presents the best candidate for mantle-derived lithologies.

Acknowledgments. The authors are most grateful to the NASA Planetary Geology and Geophysics Program, the Lunar Data Analysis Program, and the Cosmochemistry Program for support to carry out this research. Constructive reviews by Scott Murchie, Patrick Pinet, and Matt Staid strengthened the manuscript and are most appreciated. The talented assistance of Peter Neivert in preparation of several figures is gratefully acknowledged.

References

Adams, J. B., and T. B. McCord, Alteration of lunar optical properties: Age and composition effect, *Science*, *171*(3971), 567-571, 1971a.

Adams, J. B., and T. B. McCord, Optical properties of mineral separates, glass, and anorthositic fragments from Apollo mare samples, *Proc. Lunar Planet. Sci., 2nd*, 2183-2195, 1971b.

Belton, M. J. S., et al., Lunar impact basins and crustal heterogeneity: New western limb and farside data from Galileo, *Science*, *255*(5044), 570-576, 1992.

Blewett, D. T., P. G. Lucey, B. R. Hawke, and B. L. Jolliff, Clementine images of the lunar sample-return stations: Refinement of FeO and TiO_2 mapping techniques, *J. Geophys. Res.*, *102*, 16,319-16,325, 1997.

Blewett, D. T., G. J. Taylor, P. G. Lucey, B. R. Hawke, and J. Gillis, High-resolution, quantative remote sensing of South Pole-Aitken basin, *Lunar Planet. Sci.* [CD-ROM], *XXX*, abstract 1438, 1999.

Blewett, D. T., P. G. Lucey, B. R. Hawke, J. Holtzmann, G. J. Taylor, and D. J. Lawrence, Compositional studies of the South Pole-Aitken basin, *Lunar Planet. Sci.* [CD-ROM], *XXXI*, abstract 1501, 2000.

Burns, R. G., *Mineralogical Application of Crystal Field Theory*, 551, pp., Cambridge Univ. Press, New York, 1993.

Chevrel, S. D., P. C. Pinet, Y. Daydou, S. Maurice, W. C. Feldman, D. J. Lawrence, and P. G. Lucey, Fe, Ti and Th abundances of the lunar surface at global scale from UV-VIS spectral Clementine and gamma-ray lunar prospector data, *Lunar Planet. Sci.* [CD-ROM] *XXXI*, abstract 1629, 2000.

Cintala, M. J., and R. A. F. Grieve, Scaling impact melting and crater dimensions: Implications for the lunar cratering record, *Meteor. Planet. Sci.*, *33*, 889-912, 1998.

Cook, A. C., M. S. Robinson, and T. R. Watters, Planet-Wide Lunar Digital Elevation Model, *Lunar Planet. Sci.* [CD-ROM], *XXXI*, abstract 1978, 2000.

Eliason, E. M., Production of digital image models with the ISIS system, *Lunar Planet. Sci., XXVIII*, 331-332, 1997.

Eliason, E. M., C. Isbell, E. M. Lee, T. Becker, L. A. Gaddis, A. McEwen, and M. S. Robinson, The Clementine UVVIS Global Lunar Mosaic, *NASA Planet. Data Sys. CD-Rom Archive, CL-4001-4078*, 1999a.

Eliason, E. M., et al., Digital processing for a global multispectral map of the Moon from the Clementine UVVIS imaging instrument, *Lunar Planet. Sci.* [CD-ROM], *XXX*, CD-ROM, abstract 1933, 1999b.

Ferrari, A. J., Lunar gravity: A harmonic analysis, *J. Geophys. Res.*, *82*, 3065-3084, 1977.

Gaddis, L. A., A. McEwen, and T. Becker, Compositional variations on the Moon: Recalibration of Galileo solid-state imaging data for the Orientale region and farside, *J. Geophys. Res.*, *100*, 25,345-26,355, 1995.

Gaddis, L. A., et al., An Overview of the Integrated Software for Imaging Spectrometers (ISIS), *Lunar Planet. Sci., XXVIII*, 387-388, 1997.

Gaddis, L. A., B. R. Hawke, M. S. Robinson, and C. Coombs, Compositional analyses of small lunar pyroclastic deposits using Clementine multispectral data, *J. Geophys. Res.*, *105*, 4254-4262, 2000.

Hapke, B., *Theory of Reflectance and Emittance Spectroscopy*, 455, pp., Cambridge Univ. Press, New York, 1993.

Hartman, W. K., and G. P. Kuiper, Concentric structures surrounding lunar basins, in *Lunar and Planetary Laboratory Communications*, pp. 55-66, Univ. of Ariz., Tucson, 1962.

Head, J. W., and L. Wilson, Lunar mare volcanism: Stratigraphy, eruption conditions, and the evolution of secondary crusts, *Geochim. Cosmochim Acta.*, *56*, 2155-2175, 1992.

Head, J. W., S. Murchie, J. F. Mustard, C. M. Pieters, G. Neukum, A. McEwen, R. Greeley, E. Nagel, and M. J. S. Belton, Lunar impact basins: New data for the western limb and far side (Orientale and

South Pole-Aitken basins) from the first Galileo flyby, *J. Geophys. Res.*, *98*, 17,149-17,181, 1993.

Head, J. W. I., L. Wilson, and C. M. Pieters, Pyroclastic Eruptions associated with the Floor-Fractured Lunar Farside Crater Oppenheimer in the South Pole Aitken Basin, *Lunar Planet. Sci.* [CD-ROM], *XXXI*, abstract 1280, 2000.

Heiken, G. H., D. T. Vaniman, and B. M. French (Eds.), *Lunar Sourcebook, A User's Guide to the Moon*, 736, pp., Cambridge Univ. Press, New York, 1991.

Hillier, J. K., B. J. Buratti, and K. Hill, Multispectral photometry of the Moon and absolute calibration of the Clementine UV/VIS camera, *Icarus 141*, 205-225, 1999.

Howard, K. A., D. E. Wilhelms, and D. H. Scott, Lunar basins formation and highland stratigraphy, *Rev. Geophys., 12*, 309-327, 1974.

Jolliff, B. L., J. J. Gillis, L. A. Haskin, R. L. Korotev, and M. A. Wieczorek, Major lunar crustal terranes: Surface expression and crust-mantle origins, *J. Geophys. Res.*, *105*, 4197-4216, 2000.

Kaula, W. M., R. E. Schubert, R. E. Lingenfelter, W. L. Sjogren, and W. R. Wollenhaupt, Lunar topography from Apollo 15 and 16 laser altimetry, *Proc. Lunar Planet. Sci. 4th*, *3*, 2811-2819, 1973.

Kislyuk, V. S., Profile of the far side of the Moon using Zond-8 data, *Astromet. Astrofiz.*, 31-36, 1975.

Lawrence, D. J., W. C. Feldman, B. L. Barraclough, A. B. Binder, R. C. Elphic, S. Maurice, and D. R. Thomsen, Global elemental maps of the Moon: The lunar prospector gamma-ray spectrometer, *Science*, *281*, 1484-1489, 1998.

Lawrence, D. J., W. C. Feldman, B. L. Barraclough, A. B. Binder, R. C. Elphic, S. Maurice, M. C. Miller, and T. H. Prettymman, Thorium abundances on the lunar surface, *J. Geophys. Res., 105*, 20,307-20,331, 2000.

Le Mouelic, S., Y. Langevin, S. Erard, P. C. Pinet, S. D. Chevrel, and Y. Daydou, Discrimination between maturity and composition of lunar soils from integrated Clementine UV-visible/near-infrared data: Application to the Aristarchus Plateau, *J. Geophys. Res.*, *105*, 9445-9455, 2000.

Leikin, G. A., and A. N. Sanovich, Origin of the southern basin on the far side of the Moon, *Astron. Vestnik*, *19*, 113-119, 1985.

Li, L., J. F. Mustard, and C. M. Pieters, The effects of scattered light in the Clementine UV-VIS camera on mixture analysis, *Lunar Planet. Sci.*, [CD-ROM], *XXX*, abstract 1866, 1999.

Lucey, P. G., P. D. Spudis, M. Zuber, D. Smith, and E. Malaret, Topographic-compositional units on the Moon and the early evolution of the lunar crust, *Science*, *266*, 1855-1858, 1994.

Lucey, P. G., G. J. Taylor, and E. Malaret, Abundance and distribution of iron on the Moon, *Science*, *268*, 1150-1153, 1995.

Lucey, P. G., D. T. Blewett, and B. R. Hawke, Mapping the FeO and TiO_2 content of the lunar surface with multispectral imagery, *J. Geophys. Res.*, *103*, 3679-3699, 1998a.

Lucey, P. G., et al., Calibration of the Clementine near infrared camera: Ready for prime time, *Lunar Planet. Sci.* [CD-ROM], *XXIX*, abstract 1576, 1998b.

Lucey, P. G., G. J. Taylor, B. R. Hawke, and P. D. Spudis, FeO and Ti02 concentrations in the South Pole-Aitken basin: Implications for mantle composition and basin formation, *J. Geophys. Res.*, *103*, 3701-3708, 1998c.

Lucey, P. G., D. T. Blewett, and B. L. Joliff, Lunar iron and titanium abundance algorithms based on final processing of Clementine untraviolet-visible images, *J. Geophys. Res.*, *105*, 20,297-20,305, 2000a.

Lucey, P. G., D. T. Blewett, G. J. Taylor, and B. R. Hawke, Imaging of lunar surface maturity, *J. Geophys. Res.*, *105*, 20,377-20,386, 2000b.

McEwen, A. S., A precise lunar photometric function, *Lunar Planet. Sci., XXVII*, 841-842, 1996.

McEwen, A. S., E. M. Eliason, P. G. Lucey, E. Malaret, C. M. Pieters, M. S. Robinson, and T. Sucharski, Summary of radiometric calibration and photometric normalization steps for the Clementine UVVIS images, *Lunar Planet. Sci.* [CD-ROM], *XXIX*, abstract 1466, 1998.

Metzger, A. E., J. I. Trombka, R. C. Reedy, and J. R. Arnold, Element concentrations from lunar orbital gamma-ray measurements, *Geochim. Cosmochim. Acta, Suppl. 5*(2), 1067-1078, 1974.

Morrison, D. A., and D. B. J. Bussey, The Apollo and Korolev basins and the stratigraphy of the lunar crust, *Lunar Planet. Sci.* [CD-ROM], *XXVIII*, abstract 1501, 1997.

Morrison, D. A., Did a Thick South Pole-Aitken Basin Melt Sheet Differentiate to form Cumulates?, *Lunar Planet. Sci.* [CD-ROM], *XXIX*, abstract 1657, 1998.

Mustard, J. F., and J. W. I. Head, Buried stratigraphic relationships along the southwestern shores of Oceanus Procellarum: Implications for early lunar volcanism, *J. Geophys. Res.*, *101*, 18,913-18,925, 1996.

Neumann, G. A., M. T. Zuber, D. E. Smith, and F. G. Lemoine, The lunar crust: Global structure and ignature of major basins, *J. Geophys. Res.*, *101*, 16,841-16,863, 1996.

Nozette, S., et al., The Clementine Mission to the Moon: Scientific overview, *Science*, *266*, 1835-1839, 1994.

Otake, H., J. Haruyama, and T. Matsunaga, Optical observations of the lunar surface from the orbiter of SELENE, *Lunar Planet. Sci., XXVIII*, 1051-1052, 1997.

Papike, J. J., F. N. Hodges, A. E. Bence, M. Cameron, and J. M. Rhodes, Mare basalts: Crystal chemistry, mineralogy, and petrology, *Rev. Geophys., 14*, 475-540, 1976.

Papike, J. J. (Ed.), *Reviews in Mineralogy*, 1014 pp., Mineral. Soc. of Am., Washington, D. C., 1998.

Petro, N. E., L. R. Gaddis, and M. I. Staid, Analysis of the Oppenheimer pyroclasic deposits using Clementine UVVIS Data, *Lunar Planet. Sci.* [CD-ROM], *XXXII*, abstract 1953, 2001.

Pieters, C. M., Compositional diversity and stratigraphy of the lunar crust derived from reflectance spectroscopy, in *Remote Geochemical Analysis: Elemental and Mineralogical Composition*, edited by C.M. Pieters and P.A.J. Englert, pp. 309-339, Cambridge Univ. Press, New York, 1993.

Pieters, C. M., The Moon as a spectral calibration standard enabled by lunar samples: The Clementine example, in *Workshop of New Views of the Moon II: Understanding the Moon Through the Integration of Diverse Datasets*, pp. 47-49, Lunar Planet. Inst., Houston, Tex., 1999.

Pieters, C. M., M. I. Staid, E. M. Fischer, S. Tompkins, and G. He, A sharper view of impact craters from Clementine data, *Science*, *266*, 1844-1848, 1994.

Pieters, C. M., G. He, M. Staid, S. Tompkins, and E. M. Fischer, Clementine UVVIS data calibration and processing, report, Brown Univ., Providence, R. I., 1997a.

Pieters, C. M., S. Tompkins, J. W. Head, and P. C. Hess, Mineralogy of the mafic anomaly in the South Pole-Aitken Basin: Implications for excavation of the lunar mantle, *Geophys. Res. Lett.*, *24*, 1903-1906, 1997b.

Pieters, C. M., L. A. Taylor, S. K. Noble, L. P. Keller, B. Hapke, R. V. Morris, C. C. Allen, D. S. McKay, and S. Wentworth, Space weathering on airless bodies: Resolving a mystery with lunar samples, *Meteor. Planet. Sci.*, *35*, 1101-1107, 2000.

Pieters, C. M., J. W. Head, L. R. Gaddis, B. L. Jolliff, and M. Duke, The character and possible origin of "Olivine Hill" in South Pole-Aitken basin, *Lunar Planet. Sci.* [CD-ROM], *XXXII*, abstract 1810, 2001.

Robinson, M. S., Scattered light in the Clementine UVVIS Camera, *Lunar Planet. Sci.* [CD-ROM], *XXXII*, abstract 2004, 2001.

Robinson, M. S., A. S. McEwen, E. M. Eliason, E. M. Lee, E. Malaret, and P. G. Lucey, Clementine UVVIS Global Mosaic: A new tool for understanding the lunar crust, *Lunar Planet. Sci.* [CD-ROM], *XXX*, abstract 1931, 1999.

Rodionov, B. N., et al., New information on lunar relief from Zond-6 photographs, *Kosm. Issled*, *9*, 450-458, 1971.

Rodionov, B. N., A. A. Nefed'ev, M. I. Shpekin, and others, Study of the relief on the far side of the Moon using Zond-8 photographs, *Kosm. Issled.*, *14*, 624-629, 1976.

Schultz, P., Forming of South Pole-Aitkin Basin: The extreme games, *Lunar Planet. Sci., XXVIII*, 1259-1260, 1997.

Scott, D. H., J. F. McCauley, and M. N. West, Geologic map of the west side of the Moon, Scale 1:5,000,000, *USGS Miscell. Invest. Ser., I-1034*, 1977

Shevchenko, V. V., Modern study of the Moon, *Moscow Sci.*, 284, 1980.

Shkuratov, Y. G., and M. A. Kreslavsky, A model of lunar photometric function, *Lunar Planet. Sci.* [CD-ROM], *XXIX*, abstract 1117, 1998.

Shkuratov, Y. G., V. G. Kaydash, C. M. Pieters, and N. V. Opanasenko, A comparison of absolute calibrations of clementine-UVVIS and earth-based data for the Moon, *Lunar Planet. Sci.* [CD-ROM], *XXXI*, abstract 1165, 2000.

Shpekin, M. I., Relief of Mare Orientale on the Moon on the basis of "Zond-6, -8" data, Candidate thesis, Kazan Univ., Kazan, Tatarstan, 1983.

Smith, D. E., M. T. Zuber, G. A. Neumann, and F. G. Lemoine, Topography of the Moon from the Clementine LIDAR, *J. Geophys. Res.*, *102*, 1591-1611, 1997.

Solomon, S. C., R. P. Comer, and J. W. Head, The evolution of impact

basins: Viscous relaxation of topographic relief, *J. Geophys. Res.*, *87*, 3975-3992, 1982.

Spudis, P. D., R. A. Reisse, and J. J. Gillis, Ancient multiring basins and the Moon revealed by Clementine Laser Altimetry, *Science*, *266*, 1848-1851, 1994.

Staid, M. I., and C. M. Pieters, Integrated spectral analysis of mare soils and craters: Applications to eastern nearside basalts, *Icarus*, *145*, 122-139, 2000.

Stoffler, D., H.-D. Knoll, U. B. Marvin, C. H. Simonds, and P. H. Warren, Recommended classification and nomenclature of lunar highland rocks--A committee report, in *Proceedings of the Conference on Lunar Highlands Crust*, edited by J.J. Papike and R.B. Merrill, pp. 51-70, Pergamon, New York, 1980.

Stuart-Alexander, D. E., Geologic map of the central far side of the Moon, Scale 1:5,000,000, *U.S. Geol. Surv., Map, I-1047*, 1978.

Tompkins, S., and C. M. Pieters, Mineralogy of the lunar crust: Results from Clementine, *Meteor. Planet. Sci.*, *34* (1), 25-41, 1999.

Torson, J., and K. Becker, ISIS - A software architecture for processing planetary images, *Lunar Planet. Sci. XXVIII*, 1443-1444, 1997.

Weitz, C. M., J. W. Head, and C. M. Pieters, Lunar regional dark mantle deposits: Geologic, multispectral, and modeling studies, *J. Geophys. Res.*, *103*, 22,725-22,759, 1998.

Weitz, C. M., M. J. Rutherford, J. W. Head, and D. S. McKay, Ascent and eruption of a lunar high-titanium magma as inferred from the petrology of the 74001/2 drill core, *Meteor. Planet. Sci.*, *34*, 527-540, 1999.

Wieczorek, M. A., and R. J. Phillips, The structure and compensation of the lunar highland crust, *J. Geophys. Res.*, *102*, 10,933-10,943, 1997.

Wieczorek, M. A., and R. J. Phillips, Potential anomalies on a sphere: Applications to the thickness of the lunar crust, *J. Geophys. Res.*, *103*, 1715-1724, 1998.

Wieczorek, M. A., and R. J. Phillips, Lunar multiring basins and the cratering process, *Icarus*, *139*, 246-259, 1999.

Wieczorek, M. A., and M. T. Zuber, The Composition of the Lunar Crust: Constraints from Central Peaks and Crustal Thickness Modeling, *Lunar Planet. Sci.* [CD-ROM], *XXXII*, abstract 1410, 2001.

Wilhelms, D., The Geologic History of the Moon, *U.S. Geol. Surv., Prof. Pap.*, 1348, 302, 1987.

Wilhelms, D. E., Preliminary interpretations of lunar geology, Initial photographic analysis, in *Analysis of Apollo 8 Photography and Visual Observations*, pp. 16-21, chap. 2, NASA, Washington, D. C., 1969.

Wilhelms, D. E., K. A. Howard, and H. G. Wilshire, Geologic map of the South Side of the Moon, Scale 1:5,000,000, *U.S. Geol. Surv. Miscell. Invest. Ser., I-1162*, 1979.

Wollenhaupt, W. R., and W. L. Sjogren, Comments on the figure of the Moon based on preliminary results from laser altimetry, *Moon*, *4*, 337-347, 1972a.

Wollenhaupt, W. R., and W. L. Sjogren, Apollo 16 laser altimeter, Apollo 16 Preliminary Science Report, *NASA Spec. Publ., SP-315*, 30-1 to 30-5, 1972b

Wollenhaupt, W. R., W. L. Sjogren, R. E. Lingenfelter, G. Schubert, and W. M. Kaula, Apollo 17 laser altimeter, Apollo 17 Preliminary Science Report, *NASA Spec. Publ., SP-330,* 33-41 to 33-44, 1973

Wood, C. A., and A. W. Gifford, Evidence for the lunar big backside basin, in *Multi-Ring Basins: Formation and Evolution Conference*, contrib. 414, pp. 121-123, Lunar Planet. Lab., Tucson, Ariz., 1980.

Yingst, R. A., and J. W. Head, Volumes of lunar lava ponds in South Pole-Aitken and Orientale Basins: Implications for eruption conditions, transport mechanisms, and magma source regions, *J. Geophys. Res.*, *102*, 10,909-10,931, 1997.

Yingst, R. A., and J. W. Head, Geology of mare deposits in South Pole-Aitken basin as seen by Clementine UVVIS data, *J. Geophys. Res.*, *104*, 18,957-18,979, 1999.

Zhong, S., E. M. Parmentier, and M. T. Zuber, Early lunar evolution and the origin of asymmetric distribution of mare basalts, *Lunar Planet. Sci.* [CD-ROM], *XXX*, abstract 1789,

Zuber, M. T., D. E. Smith, F. Lemoine, and G. A. Neumann, The shape and internal structure of the Moon from the Clementine mission, *Science*, *266*, 1839-1843, 1994.

M. Duke, Lunar and Planetary Institute, Houston, TX 77058, USA.

L. Gaddis, U.S. Geological Survey, 2255 North Gemini Drive, Flagstaff, AZ 86001, USA.

J. W. Head III and C. M. Pieters, Department of Geological Sciences, Brown University, Providence, RI 02912, USA. (carle_pieters@brown.edu)

B. Jolliff, Department of Earth and Planetary Sciences, Washington University, One Brookings Drive, St. Louis, MO 63130, USA.

(Received October 11, 2000; revised April 23, 2001;
accepted May 29, 2001.)